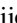# On the Effects of UV Photons/X-Rays on the Chemistry of the Sgr B2 Cloud

J. Armijos-Abendaño[1] , J. Martín-Pintado[2], E. López[1], M. Llerena[1,3] , N. Harada[4], M. A. Requena-Torres[5], S. Martín[6,7] ,
V. M. Rivilla[8], D. Riquelme[9], and F. Aldas[1]

[1] Observatorio Astronómico de Quito, Escuela Politécnica Nacional, Interior del Parque La Alameda, 170136, Quito, Ecuador; jairo.armijos@epn.edu.ec
[2] Centro de Astrobiología (CSIC, INTA), Ctra a Ajalvir, km 4, E-28850, Torrejón de Ardoz, Madrid, Spain
[3] Departamento de Física y Astronomía, Universidad de La Serena, Av. Juan Cisternas 1200 Norte, La Serena, Chile
[4] Academia Sinica Institute of Astronomy and Astrophysics, P.O. Box 23-141, Taipei 10617, Taiwan
[5] Department of Astronomy, University of Maryland, College Park, MD 20742, USA
[6] European Southern Observatory, Alonso de Córdova 3107, Vitacura, Santiago, Chile
[7] Joint ALMA Observatory, Alonso de Córdova 3107, Vitacura, Santiago, Chile
[8] INAF/Osservatorio Astrofisico di Arcetri, Largo Enrico Fermi 5, I-50125, Florence, Italy
[9] Max-Planck-Institut für Radioastronomie, Auf dem Hügel 69, D-53121 Bonn, Germany
Received 2020 January 6; revised 2020 April 23; accepted 2020 April 24; published 2020 May 26

Abstract

The lines of HOC^+, HCO, and CO^+ are considered good tracers of photon-dominated regions (PDRs) and X-ray-dominated regions. We study these tracers toward regions of the Sgr B2 cloud selected to be affected by different heating mechanisms. We find the lowest values of the column density ratios of HCO^+ versus HOC^+, HCO, and CO^+ in dense H II gas, where UV photons dominate the heating and chemistry of the gas. The HOC^+, HCO, and CO^+ abundances and the above ratios are compared with those of chemical modeling, finding that high-temperature chemistry, a cosmic-ray ionization rate of 10^{-16} s^{-1}, and timescales $>10^{5.0}$ yr explain well the HOC^+ abundances in quiescent Sgr B2 regions, while shocks are also needed to explain the highest HCO abundances derived for these regions. The CO^+ is mainly formed in PDRs, since the highest CO^+ abundances of $\sim(6\text{–}10) \times 10^{-10}$ are found in H II regions with electron densities >540 cm^{-3} and CO^+ emission is undetected in quiescent gas. Among the ratios, the HCO^+/HCO ratio is sensitive to the electron density, as it shows different values in dense and diffuse H II regions. We compare SiO $J = 2\text{–}1$ emission maps of Sgr B2 with X-ray maps from 2004 and 2012. One known spot shown on the 2012 X-ray map is likely associated with molecular gas at velocities of 15–25 km s^{-1}. We also derive the X-ray ionization rate of $\sim10^{-19}$ s^{-1} for Sgr B2 regions pervaded by X-rays in 2004, which is quite low to affect the chemistry of the molecular gas.

Unified Astronomy Thesaurus concepts: Galaxy nuclei (609); Interstellar medium (847); Photodissociation regions (1223); Molecular clouds (1072)

1. Introduction

One of the key issues in extragalactic astrophysics is the search for molecular tracers of the heating mechanisms in nearby galactic nuclei (Usero et al. 2004; Fuente et al. 2006; Martín et al. 2009b). These tracers could be used as probes of the heating sources to disentangle the type of activity in more distant galaxies. As a result of years of investigation, several molecular tracers have been proposed to discriminate between the main heating sources in active galaxies (Martín et al. 2009a, 2015). Whereas galaxies hosting active galactic nuclei (AGNs) are affected by hard X-rays arising from the accretion disks of supermassive black holes, the chemistry and heating of starburst galaxies are dominated by shocks, UV radiation, and/or cosmic rays, depending on the evolutionary stage of their nuclei (Aladro et al. 2011). However, this picture is not simple, since extragalactic observations, even in the case of the closest galaxies, do not have the necessary spatial resolution to isolate the effects of the different heating sources. Located at only 7.9 kpc (Boehle et al. 2016), the Galactic center (GC) offers an unique opportunity to study a galactic nucleus in detail. This proximity allows one to discriminate regions according to the main heating source affecting the molecular gas.

The emission lines of HCO and HOC^+ are considered to be good tracers of both photon-dominated region (PDR) and X-ray-dominated region (XDR) chemistries (Ziurys & Apponi 1995; Apponi et al. 1999; Usero et al. 2004; Martín et al. 2009b). The abundance of CO^+ is thought to be enhanced in regions affected by strong UV and X-ray radiation fields (Fuente et al. 2006; Spaans & Meijerink 2007). High abundances of HCO and HOC^+ have been found in NGC 1068, which is considered a prototypical extragalactic XDR (Usero et al. 2004). In the starburst galaxies M82 and NGC 253, HCO, HOC^+, and CO^+ are abundant (Fuente et al. 2006; Martín et al. 2009b; Aladro et al. 2015).

The HOC^+(1–0) line was detected toward the circumnuclear disk of the NGC 1808 galaxy, where the chemistry of HOC^+ may be affected by PDRs or XDRs (Salak et al. 2018). The 3–2 transition of HOC^+ shows emission from a very compact region close to the nucleus of the ultraluminous infrared galaxy (ULIRG) Mrk 273, unlike the 1–0 and 3–2 transitions of HCN, HNC, and HCO^+ that show a more extended emission, suggesting that the chemistry of HOC^+ is different from that of the other molecules (Aladro et al. 2018). The HOC^+ emission traces the molecular cloud layers most exposed to the UV radiation in the Orion bar (Goicoechea et al. 2017).

The CO^+ emission is tracing the layers between the H II region and the molecular gas in the Mon R2 star-forming region (Treviño-Morales et al. 2016). Formation of CO^+ is expected in dense regions affected by high-UV fields (Treviño-Morales et al. 2016).

The 6.4 keV Fe Kα line is considered to be an excellent tracer of XDRs, as this line arises from fluorescence when high-energy X-rays and/or particles (>7.1 keV) interact with neutral or partially ionized iron atoms (Amo-Baladrón et al. 2009). The

Table 1
Positions Observed in Sgr B2

Pos.	Heating Mechanism	$\Delta\alpha^{a}$, $\Delta\delta^{a}$ (arcsec, arcsec)
1	UV photons and/or X-rays	(0, 0)
2	UV photons and/or X-rays	(0, 60)
3	X-rays	(20, 100)
4	X-rays	(−60, 80)
5	UV photons and/or X-rays	(−110, 35)
6	X-rays	(−50, −20)
7	UV photons and/or X-rays	(−100, −90)
8	UV photons and/or X-rays	(10, −125)
9	UV photons	(−75, −225)
10	X-rays	(−250, −275)
11	X-rays	(275, −120)
12	X-rays	(275, 100)
13	Quiescent	(250, 250)

Note.
[a] Offsets are relative to the position of the massive hot core Sgr B2M ($\alpha_{J2000} = 17:47:20.40$ and $\delta_{J2000} = -28:23:07.25$).

X-ray emission toward the GC has been studied by Terrier et al. (2018) using the 6.4 keV Fe Kα line. They found that most regions they studied in the GC show bright X-ray emission in 2000–2001 that significantly decreases by 2012. Kawamuro et al. (2019) used the 6.4 keV Fe Kα line to map the X-ray-irradiated gas toward the $\sim$100 pc central region of the Circinus galaxy.

So far, it is unclear to what extent the proposed PDR and/or XDR tracers, HCO, HOC^{+}, and CO^{+}, may be used to disentangle the PDR and XDR environments in galactic nuclei. In this paper, we will try to address the above ambiguity by studying these molecular tracers in spatially resolved regions affected by X-rays and/or UV radiation in the Sgr B2 cloud. We have chosen 13 positions for our study. In Table 1, we give the heating mechanisms that affect the sources included in this paper. Positions 1, 2, 5, 7, and 8 were selected toward the 20 cm emission peaks shown in the top panel of Figure 1; therefore, the chemistry and heating of the gas in these regions would be dominated by the UV radiation. In Section 4.2, we will see that these regions can be classified into H II regions of diffuse or dense gas. As seen in the middle panel of Figure 1, the gas in positions 1–8 and 10–12 is pervaded by X-ray emission above 6σ, while that in 9 and 13 is not. The possible effects of X-rays on the chemistry of several of these Sgr B2 positions will be studied and discussed in Sections 3 and 5.1, respectively.

2. Observations and Data Reduction

Our study was performed by using data obtained with the IRAM 30 m telescope[10] at Pico Veleta (Spain) and archive data taken with the XMM-Newton space telescope.

2.1. IRAM 30 m Observations

With the IRAM 30 m telescope, we observed the HCO, HOC^{+}, and CO^{+} lines (listed in Table 2) in 2014 December toward 13 selected positions (Program 137-14; PI: Armijos-Abendaño) whose offsets relative to the massive hot core Sgr B2M position

(with $\alpha_{J2000} = 17:47:20.40$ and $\delta_{J2000} = -28:23:07.25$) are indicated in Table 1 and Figure 1. The Eight MIxer Receiver (EMIR) was used during our observations, tuning horizontal and vertical polarizations in the E090 and E230 bands, while the Fast Fourier Transform Spectrometer (FTS) and Wideband Line Multiple Autocorrelator (WILMA) were used as back ends. The FTS back end worked at a resolution of 200 kHz. We used position switching as the observing mode with the emission-free reference position $\alpha_{J2000} = 17:46:23.0$ and $\delta_{J2000} = -28:16:37.3$, which was selected from the maps of the CS molecule by Bally et al. (1987). An on-source integration time of 30 minutes was used for each position. Spectra were calibrated by using ambient and cold temperature loads, which provided a calibration accuracy of around 10%. The spatial resolution provided by the IRAM telescope, which allowed us to spatially separate PDRs, XDRs, and quiescent regions (see Figure 1), is listed in Table 2. The output spectra obtained from the IRAM 30 m telescope are calibrated in the antenna temperature scale (T_{a}^{*}), which we converted to the main-beam temperature (T_{mb}) using the relation $T_{mb} = (F_{eff}/B_{eff})T_{a}^{*}$, where F_{eff} is the forward efficiency and B_{eff} is the main-beam efficiency. The B_{eff} values were calculated using the Ruze formula $B_{eff} = 1.2\ \epsilon\,e^{-(4\pi R\sigma/\lambda)^{2}}$, where $\epsilon = 0.69$ and $R\sigma = 0.07$. We calculated B_{eff} values of 0.78–0.45 for the observed frequencies of 85–268 GHz. The F_{eff} values were taken from the online documentation of the IRAM 30 m telescope.[11]

The calibrated data observed in 2014 were imported into the MADCUBA software (Martín et al. 2019) for further processing. With this software, the baseline (of order 0–2) subtraction and spectrum averaging were applied. Then the spectra were smoothed to a velocity resolution of $\sim$5 km s^{-1}, appropriate to resolve the typical line widths observed in the GC. The rms noise level of the spectra is $\sim$10–15 mK in the T_{mb} scale.

In our study, we also used on-the-fly (OTF) data observed in 2006 August (Program 012–06; PI: Martín-Pintado). With this observing mode, we mapped a region of 15′ × 14′ within the Sgr B2 complex. The data were calibrated using the standard dual-load system. The A100 and B100 receivers connected to the 1 MHz filter bank were used in our observations, covering the frequencies of the SiO $J = 2$–1, C^{18}O $J = 1$–0, H^{13}CO^{+} $J = 1$–0, and HCO $1_{0,1}$–$0_{0,0}$ ($J = 3/2$–1/2, $F = 2$–1) transitions. Our OTF observations of HCO $1_{0,1}$–$0_{0,0}$ cover a region of 9′ × 9′, which is smaller than that mapped in the other molecular lines (see Figures 1 and 2). The data reduction was done with the GILDAS software,[12] which was also used to build the SiO $J = 2$–1, H^{13}CO^{+} $J = 1$–0, and HCO $1_{0,1}$–$0_{0,0}$ data cubes with half-power beams of $\sim$28″. The data cubes of SiO, H^{13}CO^{+}, C^{18}O, and HCO have an rms noise level of $\sim$25 mK in the T_{a}^{*} scale ($\sim$30 mK in T_{mb}). Contours tracing the SiO $J = 2$–1 emission integrated in two velocity ranges are shown in Figure 1. Integrated intensity maps of the HCO $1_{0,1}$–$0_{0,0}$ and H^{13}CO^{+} $J = 1$–0 lines are shown in Figure 2. The C^{18}O $J = 1$–0 spectra extracted over 22″ regions at selected positions will be used later to derive molecular abundances.
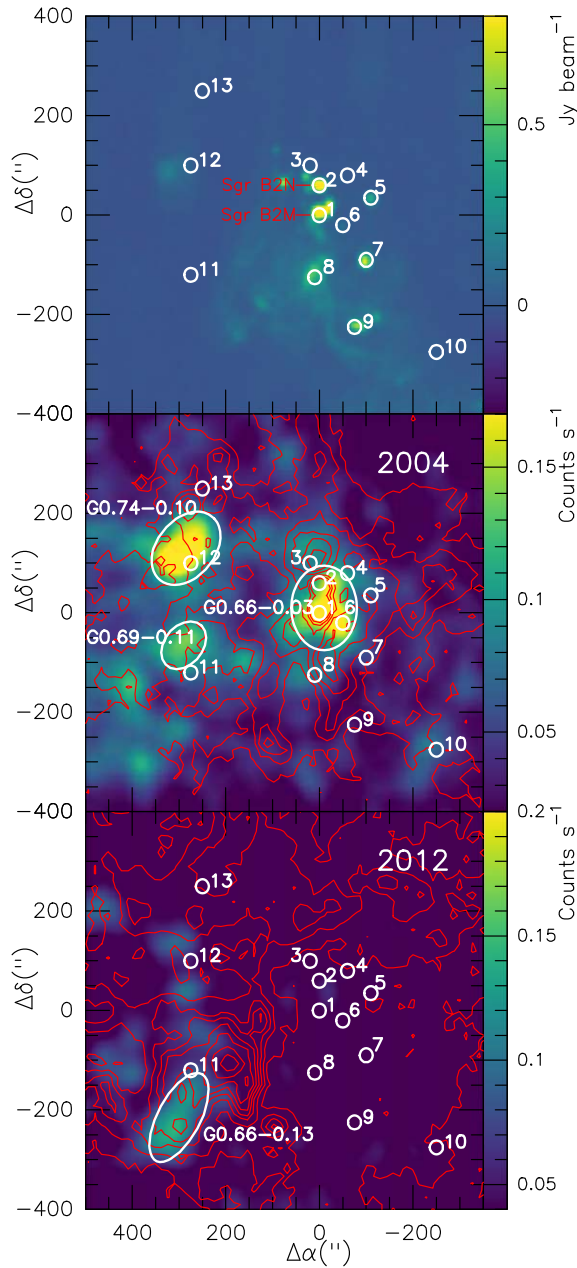
2.2. XMM-Newton Observations and Data Reduction

We have used observations available in the XMM-Newton archive to study the X-ray emission from Sgr B2. The selected

---

[10] IRAM is supported by INSU/CNRS (France), MPG (Germany), and IGN (Spain).

[11] http://www.iram.es/IRAMES/mainWiki/Iram30mEfficiencies
[12] http://www.iram.fr/IRAMFR/GILDAS

Figure 1. In the top panel, the 13 positions studied in this paper are indicated by circles with the size of the 30 m IRAM telescope beam of 28″ at 86 GHz on the Sgr B2 radio continuum map at 20 cm (Yusef-Zadeh et al. 2004). Positions 1 and 2 trace dense H II regions toward Sgr B2M (it is the origin of the offsets in arcseconds) and Sgr B2N, respectively; positions 3, 5, and 7–9 trace diffuse H II regions; and positions 4, 6, and 10–13 trace regions of quiescent gas (see Section 4.2). The gas in positions 4, 6, and 10–12 is pervaded by X-rays (see middle panel); however, the effects of X-rays on the gas in these five positions are negligible (see Section 5.1), thus these regions are considered quiescent. The middle and bottom panels are the same as the top panel, but the positions are overlapped on the 6.3–6.5 keV color maps observed in 2004 (middle panel) and 2012 (bottom panel), where the G0.66–0.03, G0.74–0.10, and G0.66–0.13 sources studied in Terrier et al. (2018) are highlighted with big white ellipses. We called the X-ray source observed in 2004 G0.69–0.11. Contours show the SiO $J = 2–1$ emission integrated over the velocity ranges of 65–75 and 15–25 km s^{-1} in the middle and bottom panels, respectively (see Section 3). Contour levels start at 1 K km s^{-1} (3σ) and increase in 2.2 K km s^{-1} steps in both velocity ranges.

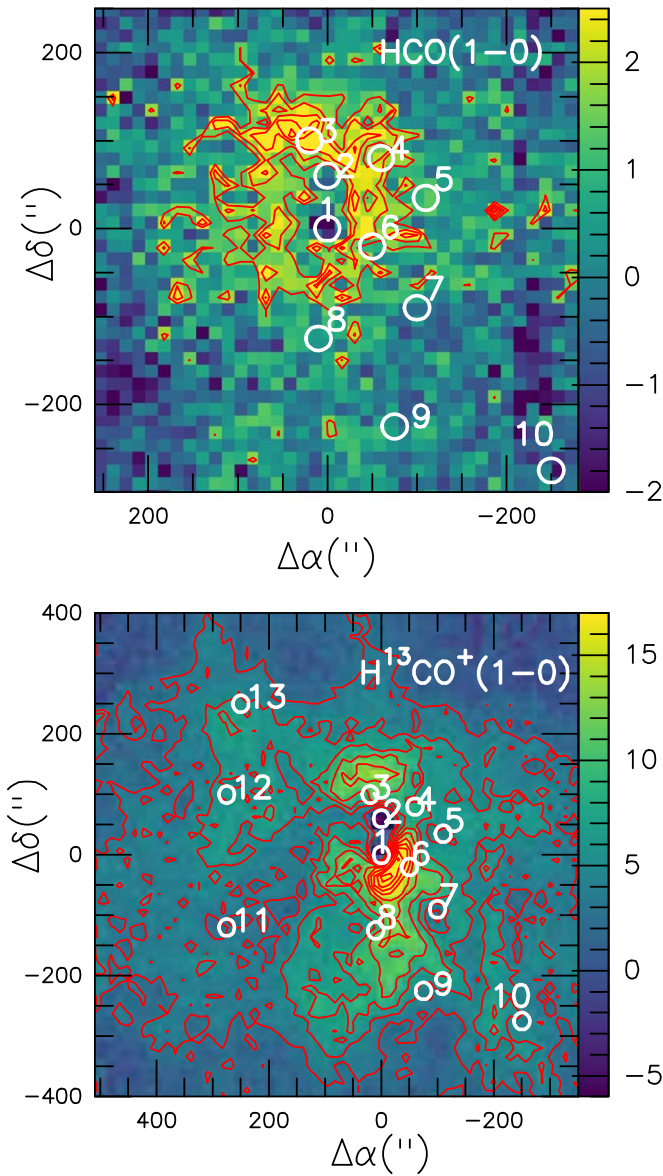| Lines	ν (GHz)	E_u (K)	HPBW (arcsec)
HCO($1_{0,1} - 0_{0,0}$)[a]	86.671	4.18	28.3
HCO($3_{0,3} - 2_{0,2}$)[b]	260.060	24.98	9.5
HOC$^+$(1–0)	89.487	4.29	27.6
HOC$^+$(3–2)	268.451	25.77	9.2
CO$^+$($J = 2–1$, 3/2-3/2)	235.380	19.96	10.5
CO$^+$($J = 2–1$, 5/2-3/2)	236.062	17.00	10.4
HC^{18}O$^+$(1–0)	85.162	4.09	28.9
HC^{18}O$^+$(3–2)	255.480	24.52	9.6
C^{18}O(1–0)	109.782	5.27	22.4
SiO(2–1)	86.847	6.25	28.3
H^{13}CO$^+$(1–0)	86.754	4.16	28.4
H42α	85.688	⋯	28.7

Notes.
[a] Formed by four hyperfine lines, but only the frequency of the most intense of the four lines is given.
[b] Formed by six hyperfine lines, but only five of the six lines were observed, and the frequency of the most intense of the five lines is given.

have exposure times of 50,918 and 41,921 seconds, respectively. The emchain task of the Science Analysis Software (SAS; version 16.1.0) was used to run the default pipeline processing, as well as to obtain the calibrated event lists, which were cleaned for flaring events. Then, the evselect task of SAS was used to extract the two images in the range of 6.3–6.5 keV shown in Figure 1. This energy range is chosen with the aim of mapping the 6.4 keV Fe line emission and the underlying continuum from Sgr B2.
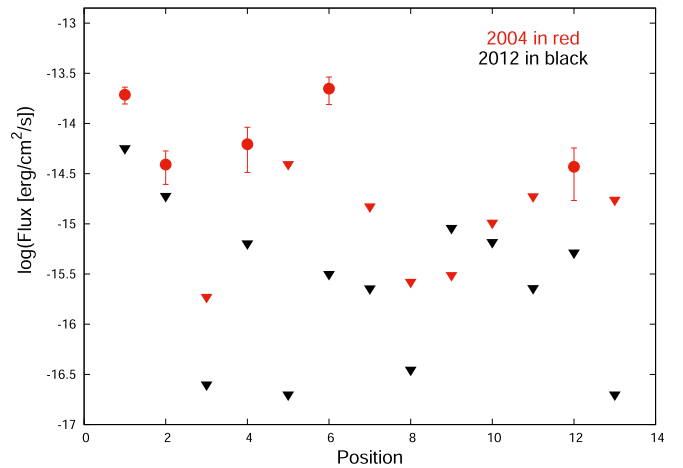
3. Analysis and Results of the X-Ray Data

The X-ray emission in the 6.3–6-5 keV range is shown in Figure 1, where contours show the SiO $J = 2–1$ emission in the velocity ranges of 65–75 and 15–25 km s^{-1} in the middle and bottom panels, respectively. The SiO $J = 2–1$ emission in the range of 65–75 km s^{-1} better matches the 2004 X-ray features toward the Sgr B2M (position 1) and Sgr B2N (position 2) hot cores, while the SiO $J = 2–1$ emission in the range of 15–25 km s^{-1} coincides well with the brightest feature in the 2012 X-ray map. The X-ray map observed in 2004 shows several emission sources (G0.66–0.03, G0.74–0.10, and G0.66–0.13) studied in Terrier et al. (2018). The selected 13 positions observed with the IRAM 30 m telescope are indicated on the X-ray maps in Figure 1. As mentioned, positions 1–12 were selected for our study, as their chemistry seems to be affected by UV photons and/or X-rays, while position 13 traces quiescent gas. In the 2004 X-ray map, G0.66–0.03 and G0.74–0.10 match several positions observed with the IRAM 30 m telescope. Associated with the Sgr B2 core (Terrier et al. 2018), G0.66–0.03 matches our observed positions 1–8, while the location of G0.74–0.10 overlaps with position 12 (see Figure 1). As seen in Figure 1, positions 10 and 11 also overlap with the X-ray emission. All of these positions overlap with the X-ray emission above 6σ. There is a third large X-ray feature that has not been labeled before, located just north of position 11, that we name G0.69–0.11. On the other hand, G0.66–0.13 on the 2012 X-ray map is located just south of position 11. It seems to be associated with the southeast region of the shell shown by the SiO $J = 2–1$ emission at 15–25 km s^{-1} (see

data were observed with the EPIC/MOS instruments in 2004 (ObsID: 0203930101; PI: Decourchelle) and 2012 (ObsID: 0694640601; PI: Terrier). The data taken in 2004 and 2012

Figure 2. Top panel: Sgr B2 emission distribution of the HCO $1_{0,1}$–$0_{0,0}$ ($J = 3/2$–$1/2$, $F = 2$–1) line integrated over the velocity range of 40–80 km s^{-1}. We show positions 1–10 studied in this paper as circles with the size of the 30 m IRAM telescope beam of $28''$ at 86 GHz. Positions 11–13 are outside the region mapped in the HCO($1_{0,1}$–$0_{0,0}$) line. Position 1 corresponds to Sgr B2M and is the origin of the offsets in arcseconds. Contours in red start at 1.6 K km s^{-1} (2σ) and increase in 0.6 K km s^{-1} steps. The wedge at the right side of the panel indicates the intensity scale in K km s^{-1}. Positions 11–13 are not drawn in the HCO($1_{0,1}$–$0_{0,0}$) map as these three positions are outside the mapped region. Bottom panel: same as the top panel, but the positions are drawn on the emission of the H^{13}CO^{+} $J = 1$–0 line integrated over the same velocity range as above. Contours start at 2.7 K km s^{-1} (3σ), increasing in 2.3 K km s^{-1} steps.

Figure 3. The Fe Kα line fluxes measured toward the 13 positions of Sgr B2. Red and black symbols show the 2004 and 2012 values, respectively. Triangles in red and black show upper limits on the Fe Kα line flux.

Figure 1). The variability in the X-ray emission observed in Sgr B2 has been explained as a result of an echo from a limited number of relatively short flares that likely originated in Sgr A* (Terrier et al. 2018).

We have extracted X-ray spectra toward the 13 positions (over regions $29''$ in diameter, thus matching the highest HPBW of our IRAM 30 m observations) of Sgr B2 to measure the Fe Kα line flux shown in Figure 3. An upper limit to the Fe Kα line flux is given in this figure when the Fe

line is not detected. The Fe Kα emission line is not detected in positions 3, 5, 7–11, and 13 in the 2004 data or any of the 13 positions in the 2012 data. Figure 4 shows a sample of the X-ray spectra observed in 2004 toward positions 1, 3, 9, and 12.

We have modeled the X-ray emission arising from positions 1, 3, 9, and 12 by considering models that include hot thermal emission added to a spectrum produced by summing a power law and one Gaussian for the Fe Kα line (in the case where it is detected; otherwise, the Gaussian is omitted in the modeling). Line-of-sight absorption is also considered in the emission modeling. The best-fit models of the four positions are shown in Figure 4, and the derived parameters are listed in Table 3. Following the work of Terrier et al. (2010), the intrinsic absorption and plasma temperature are assumed to be equal to 6.8×10^{23} cm^{-2} and 5.8 keV, respectively. Both parameters together with the solar metallicity were considered as fixed parameters in our modeling.

Table 3 shows that the studied regions would be irradiated by a field of X-rays lower than $10^{37.09}$ erg s^{-1}. Positions 1, 2, 4, 6, and 12 (see Figure 3) show a decrease in the Fe Kα flux larger than $\sim$60% between 2004 and 2012. Assuming a constant decay in the X-ray flux from 2004 to 2012, the 2012 fluxes decreased an extra 15% until 2014. Regions studied toward positions 6 and 12 can be considered as source targets to study the possible effects of X-rays on the molecular gas because they do not trace ionized gas (see Section 4.2 and Figure 5) but do trace gas that has been affected by X-rays in 2004, which could have modified the chemistry of the gas toward both regions. We have also derived X-ray fluxes within $\sim$10^{-14}–10^{-13} erg s^{-1} cm^{-2} in the 2–10 keV band for all positions using our models. The possible effects of the X-rays on the chemistry of the molecular gas will be discussed in Section 5.1.

4. Analysis and Results of the Millimeter Data

4.1. Maps of HCO and H^{13}CO^{+}

As mentioned above, Figure 2 displays maps of the HCO $1_{0,1}$–$0_{0,0}$ ($F = 2$–1) and H^{13}CO^{+} $J = 1$–0 lines integrated over the velocity range of 40–80 km s^{-1}. As seen in this figure, the HCO $1_{0,1}$–$0_{0,0}$ line emission is extended and detected above
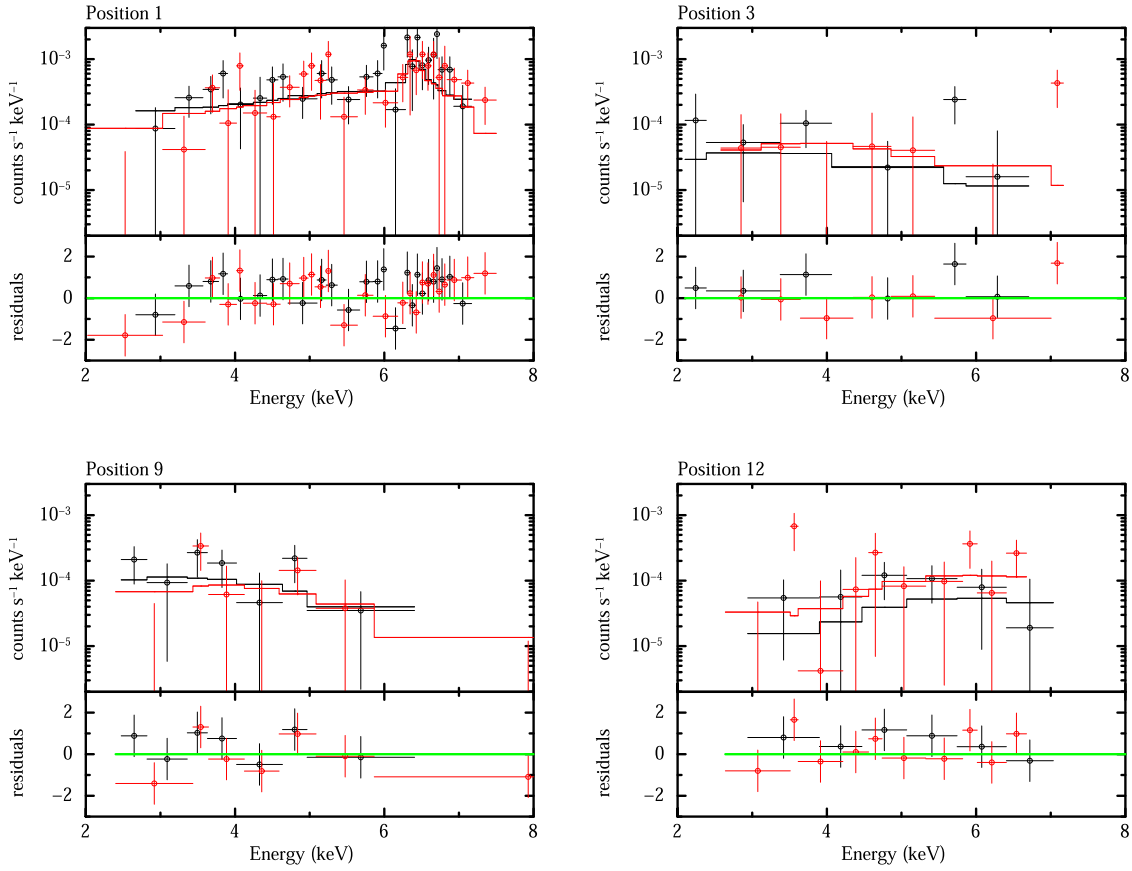
Figure 4. The X-ray spectra observed toward four positions (1, 3, 9, and 12) of Sgr B2. The red and black crosses show the XMM-Newton observations taken in 2004 with each EPIC-MOS camera, while the histograms represent the best-fit models. The lower panels in each box show the residuals normalized to the errors.

Table 3
Best-fit Results of the 2004 X-Ray Spectrum Modeling

Pos.	EW[a] (keV)	$\log(L_X$[b]$)$ (erg s^{-1})	χ^2/dof[c]
1	0.63 (<0.84)	$37.1^{+0.1}_{-0.1}$	55.38/49
3	<0.49	$35.9^{+0.3}_{-1.6}$	10.97/10
9	<0.71	$36.0^{+0.2}_{-0.5}$	17.38/10
12	0.74 (<1.42)	$36.6^{+0.2}_{-0.3}$	12.87/14

Notes.
[a] The equivalent width of the 6.4 keV Fe line.
[b] Absorption-corrected luminosity in the 2–10 keV range.
[c] Degrees of freedom.

2σ toward positions 3 and 4 and partially in position 6. As mentioned in Section 2.1, the HCO data cube has an rms level of ∼30 mK. This rms value is not enough to detect the HCO $1_{0,1}$–$0_{0,0}$ $F = 2$–1 line emission (above 2σ) toward positions 1, 2, 5, and 7–13 in our map because in Section 4.4 we notice that this HCO line has peak intensities $\lesssim$60 mK toward these 10 positions.

Figure 2 shows widespread H^{13}CO$^+$ $J = 1$–0 line emission above 3σ toward Sgr B2. Figure 1 displays widespread SiO $J = 2$–1 line emission toward Sgr B2 as well. As seen in Figures 1 and 2, the molecular emission toward Sgr B2 is extended over the beam of the 30 m IRAM telescope. Thus, in Sections 4.3–4.7, we consider a beam-filling factor of unity in the line modeling.

4.2. Ionized Hydrogen

As seen in Figure 5, we have detected line emission $\gtrsim$55 mK from the H42α radio recombination line (RRL) toward positions 1–3, 5, and 7–9 in Sgr B2. The H II regions 1–2, 5, and 7–9 were selected from the 20 cm continuum emission peaks shown in Figure 1. Following the same method as in Section 3.4 from Armijos-Abendaño et al. (2018), we have derived electron densities of 280–550 cm^{-3} for positions 3, 5, and 7–9, as well as electron densities of 1200–1700 cm^{-3} for positions 1 and 2. We have considered the sources in positions 3, 5, and 7–9 as diffuse H II regions, as their electron densities are at least a factor 2.2 lower than those of positions 1 and 2 considered as dense H II regions. Position 9 has the highest electron density of 540 cm^{-3} among all positions tracing diffuse H II gas.

There is no emission of the H42α RRL in positions 11–13, and it is very low in positions 4, 6, and 10, supporting the idea that these sources are quiescent and affected by shocks, and some of them are affected by X-rays (see Section 3). Toward these quiescent regions, we estimated electron densities lower than 180 cm^{-3}. Figure 5 reveals that the ionized gas does not have a molecular counterpart in all velocity components in positions 7–9. As will be discussed below, the C^{18}O gas has two velocity components at ∼54 and 90 km s^{-1} in positions 8 and 9, while the ionized gas shows only low velocities within ∼55–70 km s^{-1} in both positions (see Figure 5). In position 7, the C^{18}O gas shows three velocity components at ∼64, 92,
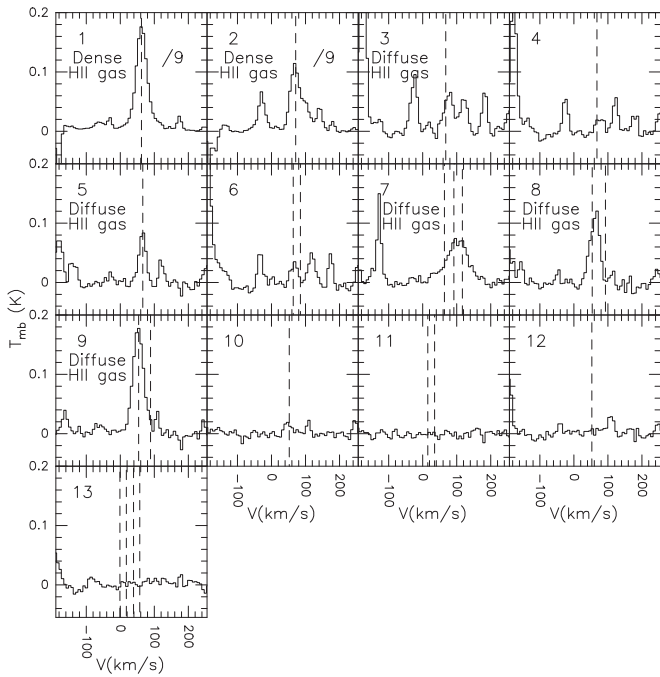
Figure 5. Spectra of the H42α RRL observed toward 13 positions of Sgr B2 (shown in Figure 1). The positions are labeled with numbers in the top left corner of each panel. Velocity components observed in the $C^{18}O$ $J = 1$–0 lines (see Section 4.6) are indicated with dashed lines for comparison between the ionized gas velocities and those of molecular gas. Positions 1 and 2 trace regions of dense H II gas with electron densities of 1200–1700 cm^{-3}, while positions 3, 5, and 7–9 trace regions of diffuse H II gas with electron densities of 280–550 cm^{-3} (see Section 4.2). Positions 1, 2, 5, and 7–9 were selected from 20 cm continuum emission peaks shown in Figure 1. The H42α line intensity in positions 1 and 2 is divided by 9 for better visualization.

and 117 km s^{-1}, whereas the H42α RRL intensity peaks at 90–120 km s^{-1}.

4.3. HOC$^+$ Molecule

Figure 6 shows the spectra of the HOC$^+$ 1–0 and 3–2 transitions toward the 13 positions studied in this paper. The HOC$^+$ 1–0 line is observed in absorption in position 1 and appears slightly absorbed in position 2. The HOC$^+$ 3–2 line is blended with hyperfine lines of $^{33}SO_2(7_{2,6}$–$6_{1,5})$. The SO_2 molecule is considered as a good tracer of hot core chemistry (Jiménez-Serra et al. 2007). As seen in Figure 6, the HOC$^+$ $J = 1$–0 emission is detected in positions 3–13, whereas the HOC$^+$ $J = 3$–2 emission above 3σ is detected only in positions 3, 4, 6, and 9.

To derive HOC$^+$ column densities (N_{tot}) and excitation temperatures, we have used the AUTOFIT tool of SLIM in the MADCUBA package (Martín et al. 2019). This tool allows us to fit synthetic spectra to the data assuming local thermodynamic equilibrium (LTE) conditions. The FWHM of the HOC$^+$ lines was fixed in the line fitting (except for the low-velocity gas of position 9). Multiple velocity components were considered in the line fitting of positions 6–9, 11, and 13. The excitation temperature (T_{ex}) in the range from 4.6 to 9.9 K is found toward several positions studied in Sgr B2 (see Table 4). The T_{ex} was fixed to the average value of 6 K when the AUTOFIT tool did not converge.

We considered Sgr B2M and Sgr B2N as blackbody emitters with a size of 2″ and a temperature of 150 K (Belloche et al. 2013) to fit the absorption line of HOC$^+$ $J = 1$–0 in positions 1 and 2, respectively. This continuum was also used in Rivilla et al. (2018) to study both sources. As mentioned above, the HOC$^+$ 3–2 emission is blended with the $^{33}SO_2$ emission. Belloche et al. (2013) explained the $^{33}SO_2$ emission in Sgr B2M (our position 1) using two components. One considers a source size of 2″, a T_{ex} of 200 K, and a column density of 1.8×10^{17} cm^{-2}, while the other considers a source size of 60″, a T_{ex} of 50 K, and a column density of 5.4×10^{13} cm^{-2}. The observed HOC$^+$ $J = 3$–2 line in position 1 was modeled using both the $^{33}SO_2$ emission from the compact component estimated by Belloche et al. (2013) and the contribution of HOC$^+$ $J = 3$–2. In this modeling, we have neglected the $^{33}SO_2$ emission contribution from the extended component, as it represents ~5% of the observed HOC$^+$ $J = 3$–2 line. An additional component for HOC$^+$ with a T_{ex} of 30 K and a column density of ~1×10^{13} cm^{-2} is needed to model the HOC$^+$ $J = 3$–2 line in position 2, in which we have not taken into account a contribution from $^{33}SO_2$, as this species has not been found in position 2 (Belloche et al. 2013). The derived parameters of HOC$^+$ are listed in Table 4.

4.4. HCO Molecule

Figure 7 displays spectra at 1 and 3 mm covering four ($F = 2$–1, 1–0, 1–1, 0–1) and five ($F = 4$–3, 3–2, 3–2, 2–1, 2–2) hyperfine transitions of HCO, respectively. The HCO $F = 2$–1 and 1–0 transitions are detected in positions 1 and 2, whereas the HCO $F = 1$–1 and 0–1 transitions are blended with the strong absorption of the $H^{13}CO^+$ $J = 1$–0 transition in both positions. The emission from the HCO $F = 2$–1, 1–0, and 1–1 transitions is detected in positions 3–13, while that of the HCO $F = 0$–1 transition is not detected in all positions. The $F = 2$–1 transition of HCO shows peak intensities ≲60 mK toward positions 1, 2, 5, and 7–13 (see Figure 7). The emission from the 1 mm HCO transitions is not observed above 3σ in positions 3–13, except that of the HCO $F = 4$–3 hyperfine transition in position 3. Spectral features of other molecules are also seen in Figure 7 and labeled in the 1 and 3 mm spectral windows of positions 1 and 3.

As in the case of the HOC$^+$ molecule, the AUTOFIT tool was used to estimate HCO column densities and excitation temperatures assuming LTE conditions. The HCO lines in positions 1 and 2 are modeled by considering the same assumptions for the background sources as in the case of HOC$^+$. The HCO shows an average T_{ex} of ~5 K derived from seven positions of Sgr B2. A warmer component of HCO with a T_{ex} of 20 K and a column density of 2×10^{14} cm^{-2} is needed to fit the low-intensity lines of HCO in positions 1 and 2. The T_{ex}, FWHM, and local standard of rest (LSR) velocity were fixed in modeling when the AUTOFIT tool did not converge in our modeling. Two velocity components are included in the line modeling of positions 6, 11, and 13. The LTE best fits to the HCO lines are shown in Figure 7, and the derived parameters are listed in Table 4. Upper limits to the column density are given in this table when there is undetected HCO emission at a given velocity.

Table 4
Derived Parameters of the Studied Molecules

Pos.	HOC$^+$				HCO				CO$^+$			
	T_{ex} (K)	V_{LSR} (km s^{-1})	FWHM (km s^{-1})	N_{tot} (×10^{12} cm^{-2})	T_{ex} (K)	V_{LSR} (km s^{-1})	FWHM (km s^{-1})	N_{tot} (×10^{13} cm^{-2})	T_{ex} (K)	V_{LSR} (km s^{-1})	FWHM (km s^{-1})	N_{tot} (×10^{13} cm^{-2})
1	4[a]	63[a]	15[a]	10.0 ± 0.5	5[a]	63[a]	13.3 ± 2.2	30.0 ± 4.5	5[a]	62[a]	14[a]	19.0 ± 8.1
2	5[a]	65[a]	15[a]	15.0 ± 1.0	5[a]	65[a]	15[a]	20.0 ± 3.5	5[a]	65[a]	15[a]	13.0 ± 4.1
3	5.8 ± 0.4	69.5 ± 0.9	20[a]	2.6 ± 0.2	4.4 ± 0.7	70.1 ± 1.8	23.1 ± 4.3	10.0 ± 2.1	5[a]	71[a]	18[a]	3.7 ± 1.8
4	5.6 ± 0.5	67.6 ± 1.0	20[a]	1.7 ± 0.2	4.4 ± 0.5	70.1 ± 0.7	18.7 ± 1.6	5.9 ± 0.6	5[b]	⋯	18[b]	<4.2[c]
5	5.2 ± 0.7	66.1 ± 1.3	20[a]	1.2 ± 0.2	4.5 ± 0.8	67.0 ± 1.0	16.6 ± 2.2	2.3 ± 0.3	5[b]	⋯	18[b]	<3.4[c]
6	6.3 ± 0.4	63.7 ± 1.0	20[a]	2.0 ± 0.2	5[a]	64 ± 1.0	18[a]	3.7 ± 0.5	5[b]	⋯	18[b]	<3.4[c]
	5.3 ± 1.1	86[a]	20[a]	1.0 ± 0.2	5[a]	85[a]	18[a]	1.4 ± 0.6	5[b]	⋯	18[b]	<3.4[c]
7	5.8 ± 1.2	61.3 ± 2.4	18[a]	0.7 ± 0.2	6.1 ± 1.4	61.2 ± 2.9	18[a]	1.2 ± 0.3	5[b]	⋯	18[b]	<3.0[c]
	4.6 ± 2.7	94[a]	18[a]	0.4 ± 0.1	5[b]	⋯	18[b]	<1.1[c]	5[b]	⋯	18[b]	<3.0[c]
	6[a]	117[a]	18[a]	0.5 ± 0.1	5[b]	⋯	18[b]	<1.1[c]	5[b]	⋯	18[b]	<3.0[c]
8	6[a]	57.8 ± 3.4	18[a]	0.5 ± 0.1	5[a]	54.0 ± 1.8	18.5 ± 4.0	3.6 ± 0.7	5[b]	⋯	18[b]	<3.2[c]
	7.3 ± 2.2	93.3 ± 4.4	18[a]	0.4 ± 0.2	5[b]	⋯	18[b]	<0.8[c]	5[b]	⋯	18[b]	<3.2[c]
9	9.9 ± 2.0	50.7 ± 1.9	19.4 ± 4.6	0.5 ± 0.1	5.3 ± 1.9	54.6 ± 3.0	15.9 ± 7.1	1.8 ± 0.7	5[a]	49.0 ± 1.4	18[a]	4.3 ± 0.6
	6[a]	88[a]	18[a]	0.2 ± 0.1	5[b]	⋯	18[b]	<0.5[c]	5[b]	⋯	18[b]	<3.0[c]
10	6[a]	48.9 ± 4.4	18[a]	0.4 ± 0.2	5[a]	55.2 ± 1.8	12.4 ± 4.7	0.8 ± 0.3	5[b]	⋯	18[b]	<3.8[c]
11	6[a]	17.8 ± 4.1	18[a]	0.6 ± 0.2	7.9 ± 1.7	4.3 ± 3.1	18[a]	0.8 ± 0.2	5[b]	⋯	18[b]	<3.0[c]
	6[a]	32[a]	18[a]	0.3 ± 0.2	5[a]	28[a]	18[a]	0.5 ± 0.3	5[b]	⋯	18[b]	<3.0[c]
12	6[a]	54.4 ± 2.7	18[a]	0.5 ± 0.1	5.9 ± 0.7	58.4 ± 1.0	12.9 ± 2.2	1.8 ± 0.3	5[b]	⋯	18[b]	<2.3[c]
13	6[a]	−4.9 ± 5.2	18[a]	0.3 ± 0.1	5[a]	0[a]	18[a]	0.8 ± 0.4	5[b]	⋯	18[b]	<2.6[c]
	6[a]	18.0 ± 4.7	18[a]	0.6 ± 0.1	5[a]	25.4 ± 4.0	18[a]	1.2 ± 0.5	5[b]	⋯	18[b]	<2.6[c]
	6[a]	41.1 ± 6.2	18[a]	0.3 ± 0.1	5[b]	⋯	18[b]	<1.0[c]	5[b]	⋯	18[b]	<2.6[c]
	6[a]	64.4 ± 4.7	18[a]	0.3 ± 0.1	5[b]	⋯	18[b]	<0.8[c]	5[b]	⋯	18[b]	<2.6[c]

Notes.
[a] Parameter fixed in the LTE analysis.
[b] Assumed parameter to derive an upper limit on the molecular column density.
[c] 3σ upper limit, as the molecular emission is not detected at the velocity shown by the HOC$^+$ emission.
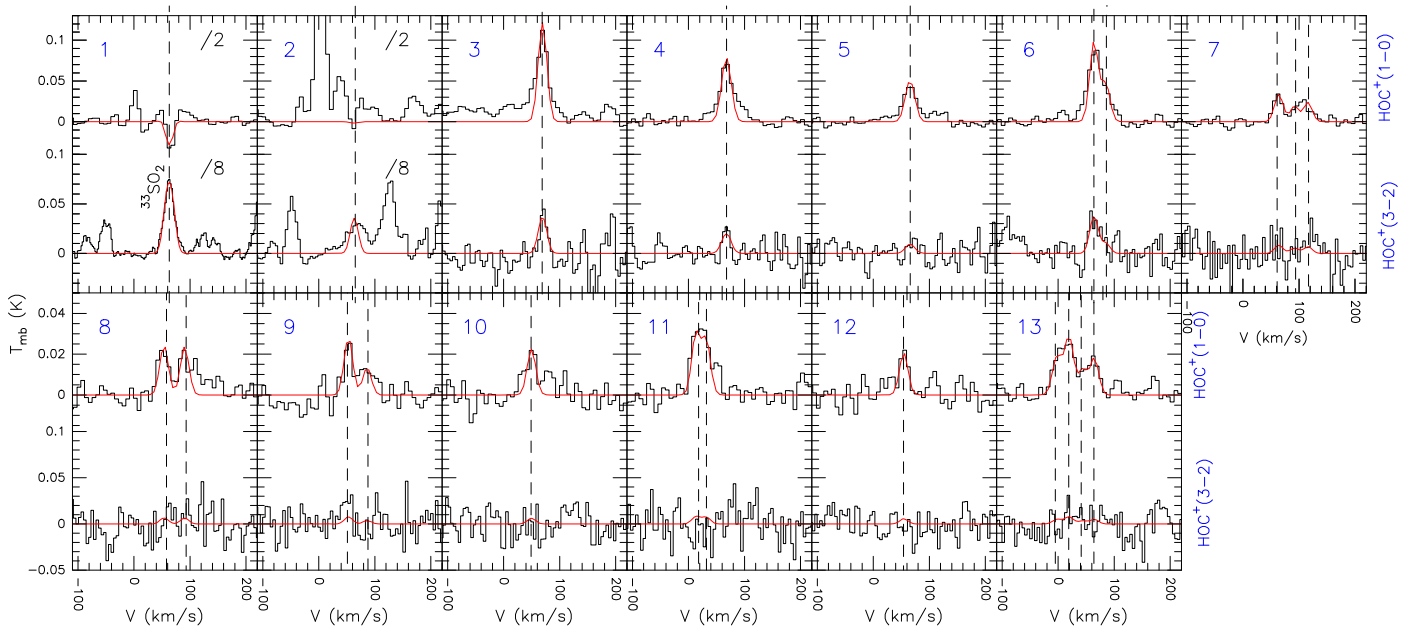
Figure 6. The HOC$^+$ J = 1–0 (top) and 3–2 (bottom) transitions observed toward 13 positions of Sgr B2 (shown in Figure 1). The positions are labeled with numbers in the top left corner of each panel. The LTE best fits to the lines obtained with MADCUBA are shown with red lines. Multiple velocity components shown with dashed lines are considered in the line fitting of positions 6–9, 11, and 13 (see Section 4.3). In positions 1 and 2, the spectra of the HOC$^+$ transitions 1–0 and 3–2 are divided by 2 and 8, respectively, for better visualization. The HOC$^+$ 3–2 line is blended with hyperfine lines of ^{33}SO$_2$($7_{2,6}$-$6_{1,5}$) in position 1 (see Section 4.3).

4.5. CO$^+$ Molecule

The CO$^+$ 5/2–3/2 and 3/2–3/2 spectra toward our studied positions of Sgr B2 are shown in Figure 8. Unfortunately, the CO$^+$ 5/2–3/2 transition is blended with two hyperfine transitions of ^{13}CH$_3$OH J = 5–4, while the CO$^+$ 3/2–3/2 transition is blended with two transitions ($12_{11,1}$–$11_{10,2}$ and $12_{11,2}$–$11_{10,1}$) of (CH$_3$)$_2$CO. The CO$^+$ lines are detected in positions 1–3 and 9, although without ambiguity only in position 9. The ambiguity in positions 1–3 is due to the line blending (see below).

We have used the AUTOFIT tool of MADCUBA to derive the CO$^+$ column density. The line fitting of the CO$^+$ lines in positions 1 and 2 is complex because of the line blending. The emission contribution from ^{13}CH$_3$OH and (CH$_3$)$_3$CO to the CO$^+$ lines cannot be ruled out in positions 1 and 2. For this reason, the lines of the three molecular species are fitted simultaneously with the AUTOFIT tool. The T_{ex} of 10 K for ^{13}CH$_3$OH and (CH$_3$)$_3$CO gives the best fits to the observed lines, which yields values of $\sim 2 \times 10^{15}$ and $\sim 2 \times 10^{16}$ cm^{-2} for ^{13}CH$_3$OH and (CH$_3$)$_3$CO, respectively. Several parameters were fixed in the CO$^+$ line fitting in all positions (see Table 4). The LTE best fits to the observed CO$^+$ lines are given in Figure 8, where the synthetic spectrum of ^{13}CH$_3$OH (and also of (CH$_3$)$_2$CO for positions 1 and 2) is shown for positions 1–4 and 6 to evidence the emission contribution of ^{13}CH$_3$OH to the CO$^+$ line. The synthetic spectrum of ^{13}CH$_3$OH is obtained considering a T_{ex} of 10 K for the five positions. The estimated parameters are given in Table 4, where an upper limit to the column density is listed in the case of undetected CO$^+$ lines.

4.6. C^{18}O Molecule

The C^{18}O J = 1–0 spectra toward the target positions of Sgr B2 are shown in Figure 9. The ground-state line of C^{18}O is included in our work as a tracer of H$_2$, allowing us to derive relative abundances of HOC$^+$, HCO, and CO$^+$. The C^{18}O

J = 1–0 lines were fitted using MADCUBA and considering multiple velocity components in several positions (see Figure 9). Using C^{18}O data, Martín et al. (2008) derived the average T_{ex} of 10 K for several positions of Sgr B2, which is considered in the C^{18}O J = 1–0 line fitting shown in Figure 9. Thus, we have derived the C^{18}O column density listed in Table 5. The H$_2$ column density (N$_{H_2}$) is also given in this table and was calculated from the column density of C^{18}O using the ^{16}O/^{18}O isotopic ratio of 250 (Wilson & Rood 1994) and the relative abundance of CO to H$_2$ of 10^{-4} (Frerking et al. 1982).

4.7. HC^{18}O$^+$ Molecule

To estimate ratios of HCO$^+$ to HOC$^+$, HCO, and CO$^+$, we have also analyzed the HC^{18}O$^+$ J = 1–0 and 3–2 spectra shown in Figure 10 toward our target positions in Sgr B2. As seen in this figure, the HC^{18}O$^+$ J = 1–0 line is detected in all positions, but the HC^{18}O$^+$ J = 3–2 line is not. The ground-state transition of HC^{18}O$^+$ is absorbed in positions 1 and 2.

As in the case of the other molecules, we have fitted synthetic spectra of HC^{18}O$^+$ J = 1–0 and 3–2 to our data to estimate the HC^{18}O$^+$ column density. The HC^{18}O$^+$ lines of positions 1 and 2 were modeled considering that Sgr B2M and Sgr B2N have continuum background sources emitting as blackbodies with similar conditions to those used for HOC$^+$. An additional warmer component of HC^{18}O$^+$ with a T_{ex} of 21 K and a column density of (0.5–1) × 10^{13} cm^{-2} is needed to fit the HC^{18}O$^+$ lines in positions 1 and 2. Multiple velocity components are taken into account in the HC^{18}O$^+$ line fitting of positions 6–9, 11, and 13. The found parameters are listed in Table 5. As seen from this table, the temperature within $\sim$6–10 K explains the excitation of HC^{18}O$^+$ toward several positions studied in Sgr B2, except the uncertain T_{ex} of 1 K required to model the absorbed HC^{18}O$^+$ J = 1–0 lines in positions 1 and 2.

In Section 5.3 we use HCO$^+$ column densities derived from the HC^{18}O$^+$ column densities given in Table 5 and using the
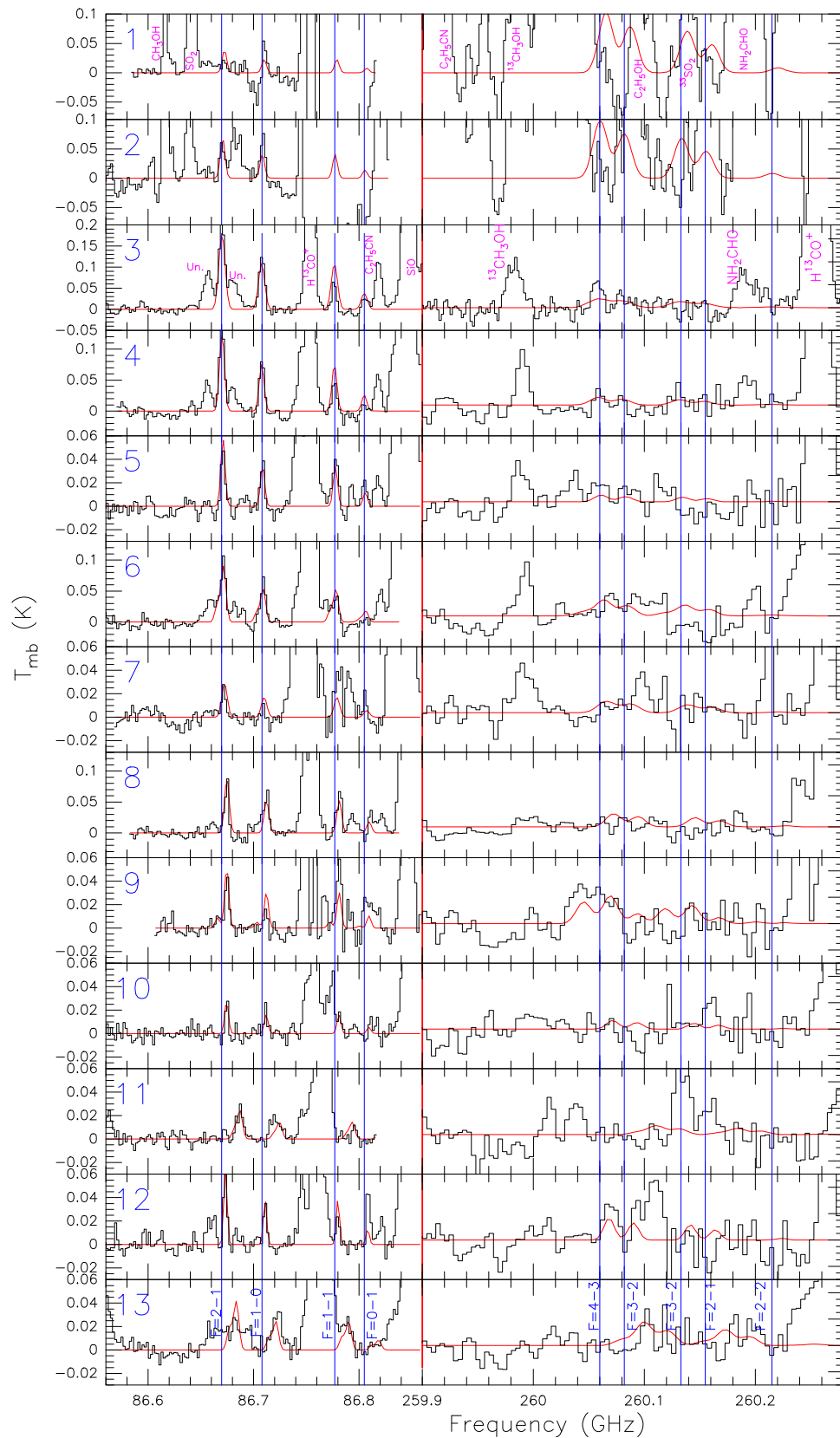
Figure 7. The HCO $F = 2–1$, $1–0$, $1–1$, $0–1$, $4–3$, $3–2$ ($J = 7/2\text{-}5/2$), $3–2$ ($J = 5/2\text{-}3/2$), $2–1$, and $2–2$ transitions (labeled in the panel of position 13) observed toward 13 positions of Sgr B2 (shown in Figure 1). The positions are labeled with numbers in the top left corner of each panel. The LTE best fits to the lines obtained with MADCUBA are shown with red lines. Blue lines indicate the frequencies of nine HCO transitions. Other identified and unidentified spectral features are shown in the panels of positions 1 and 3. The red line indicates where the 3 mm band ends.
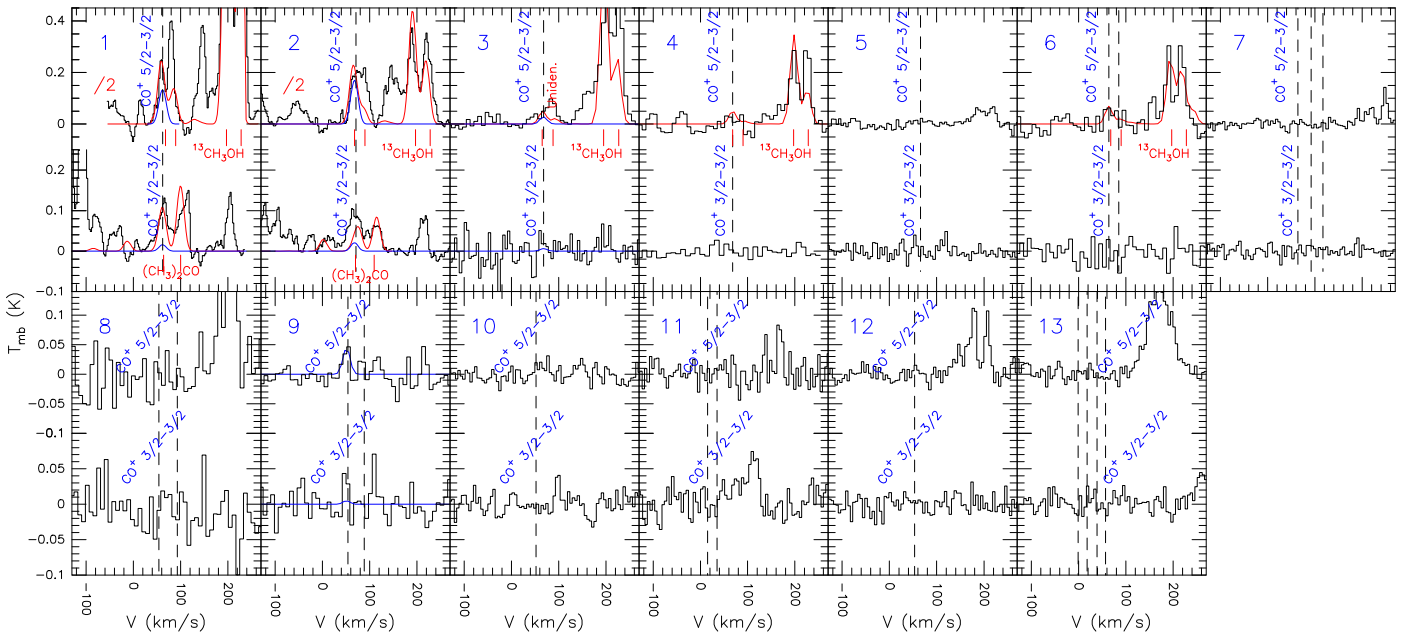
Figure 8. The CO^+ transitions observed toward 13 positions (shown in Figure 1) of Sgr B2. The positions are labeled with numbers in the top left corner of each panel. Red lines show the overall spectral fitting to the lines considering the contribution from $^{13}CH_3OH$ in positions 1–3 and $(CH_3)_2CO$ in positions 1–2. Blue lines show the contribution of the CO^+ lines to the overall spectral fitting in positions 1–3. A synthetic spectrum of $^{13}CH_3OH$ is shown in positions 4 and 6 with the aim of ruling out the presence of CO^+ emission. The positions of the four brighter transitions of $^{13}CH_3OH$ $J = 5-4$ are indicated with vertical red lines in positions 1–4 and 6, as are those of $(CH_3)_2CO$ in positions 1 and 2. Our best fit to the CO^+ lines is shown with blue lines in position 9. The fitting to the lines is explained in Section 4.5. Dashed lines represent the velocity components shown by the $C^{18}O$ $J = 1-0$ lines (see Figure 9) toward the same positions.
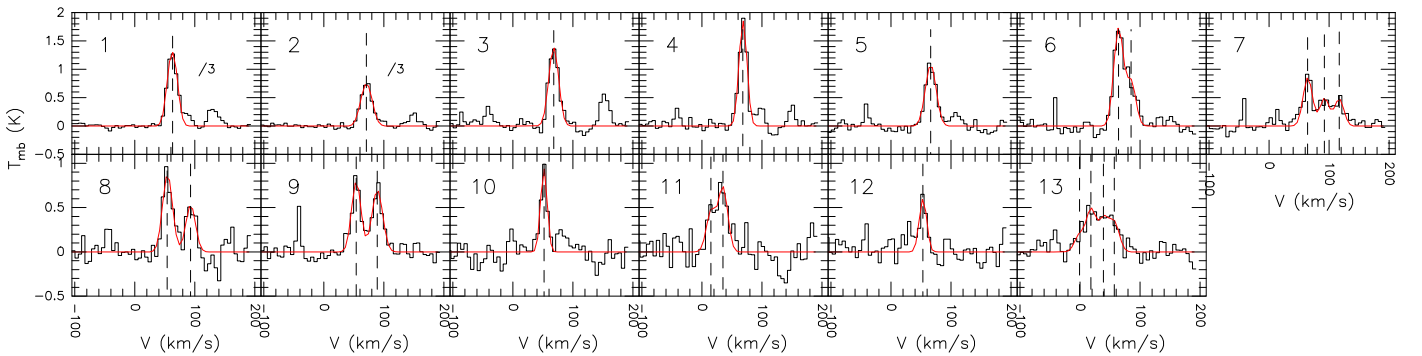
Figure 9. The $C^{18}O$ $J = 1-0$ lines observed toward 13 positions (shown in Figure 1) of Sgr B2. The positions are labeled with numbers in the top left corner of each panel. The intensity of the $C^{18}O$ $J = 1-0$ spectrum is divided by 3 toward positions 1 and 2 for better visualization. The LTE best fits to the lines obtained with MADCUBA are shown with red lines. Dashed lines represent the velocity components found from the line fitting. Multiple velocity components are identified toward positions 6–9, 11, and 13 (see Section 4.6).

$^{16}O/^{18}O$ isotopic ratio of 250 (Wilson & Rood 1994). From these HCO^+ column densities, we have also derived relative abundances of HCO^+ within $(0.5-3.2) \times 10^{-8}$ (see Figure 11) considering the H_2 column densities listed in Table 5.

5. Discussion

5.1. X-Ray Effects on the Molecular Gas?

As mentioned above, the variability in the X-ray emission in Sgr B2 could have been produced by several flares originated in Sgr A* (Terrier et al. 2010, 2018). In this scenario, Sgr B2 and other GC clouds would act as reflection clouds. Figure 1 shows that the gas mainly toward positions 1, 2, 6, and 12 was affected by X-ray emission in 2004, which may have affected the chemistry of the molecular gas. To address the possible effects of the X-rays on the molecular gas, we have calculated the X-ray ionization rate ζ_X for Sgr B2 using Equation (4)

given in Maloney et al. (1996),

$$\zeta_X \sim 1.4 \times 10^{-11} \, s^{-1} \left(\frac{L}{10^{44} \, \text{erg s}^{-1}} \right)$$

$$\times \left(\frac{r}{10^2 \, \text{pc}} \right)^{-2} \left(\frac{N_{H_2}}{10^{22} \, \text{cm}^{-2}} \right)^{-1}, \quad (1)$$

where L is the X-ray luminosity, r is the distance to the X-ray source, and N_{H_2} is the H_2 column density. We have derived $\zeta_X \sim 10^{-19} \, s^{-1}$ by considering $L \sim 10^{37} \, \text{erg s}^{-1}$ found for positions 1 and 12 in Section 3, $r = 120$ pc (the projected distance between Sgr B2 and Sgr A*), and the average column density N_{H_2} of $1 \times 10^{23} \, \text{cm}^{-2}$ estimated for positions 1, 2, 6, and 12 (see Table 5), where X-ray emission is detected in our 2004 map shown in Figure 1. The ζ_X value of $\sim 10^{-19} \, s^{-1}$ derived for Sgr B2 agrees with those shown in Figure 4 of
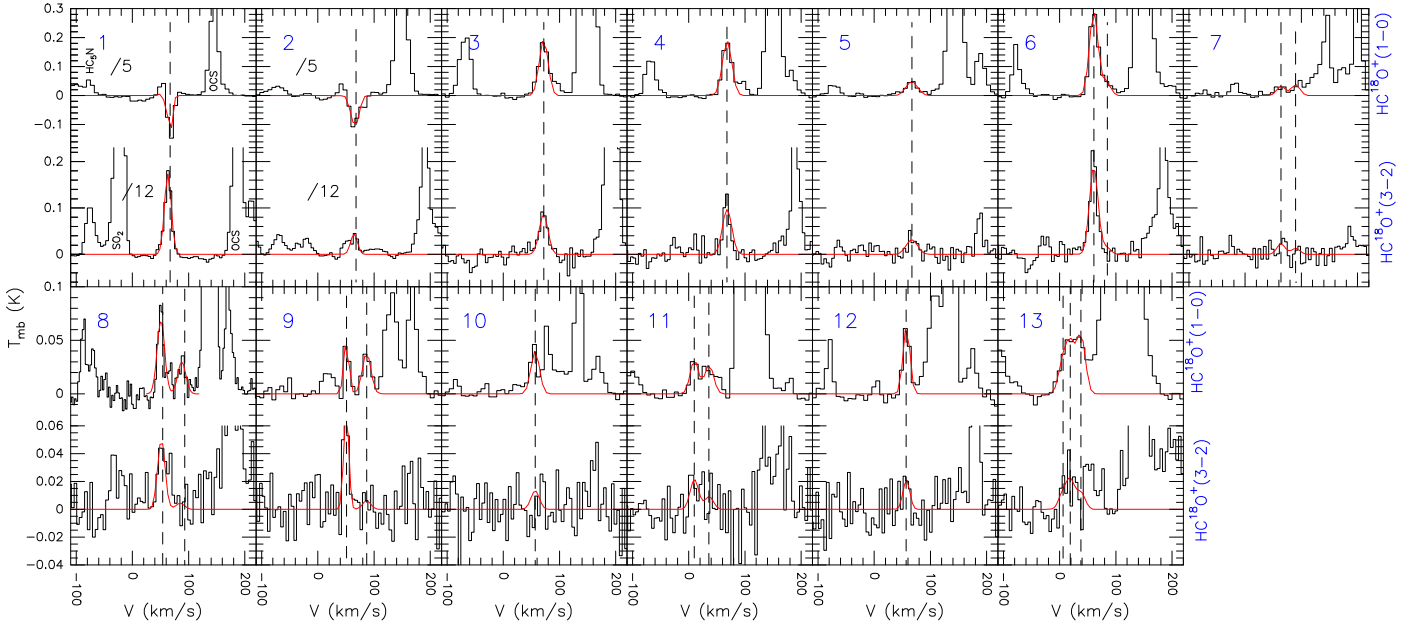
Figure 10. The $HC^{18}O^+$ $J = 1-0$ and $3-2$ lines observed toward 13 positions of Sgr B2. The positions are labeled with numbers in the top left corner of each panel. The intensity of the $J = 1-0$ and $3-2$ spectra of $HC^{18}O^+$ is divided by 5 and 12, respectively, toward positions 1 and 2 for better visualization. The LTE best fits to the lines obtained with MADCUBA are shown with red lines. Dashed lines represent the velocity components found from the line fitting. Multiple velocity components are identified toward positions 6–9, 11, and 13 (see Section 4.7). Other spectral features are labeled in the spectra of position 1.

Table 5
Derived Parameters from the $C^{18}O$ $J = 1-0$ and $HC^{18}O^+$ $J = 1-0$ Lines toward 13 Positions of Sgr B2

Pos.	$C^{18}O$				$HC^{18}O^+$			
	V_{LSR} (km s^{-1})	FWHM (km s^{-1})	N_{tot} ($\times 10^{16}$ cm^{-2})	N_{H_2} ($\times 10^{22}$ cm^{-2})	T_{ex} (K)	V_{LSR} (km s^{-1})	FWHM (km s^{-1})	N_{tot} ($\times 10^{12}$ cm^{-2})
1	62.4 ± 0.5	18.6 ± 1.2	12.0 ± 0.8	31.0 ± 2.0	1[a]	66[a]	12[a]	10.0 ± 3.2
2	70.9 ± 0.5	21.0 ± 1.0	6.8 ± 0.3	17.0 ± 0.7	1[a]	65[a]	12[a]	7.1 ± 1.6
3	67.8 ± 0.5	18.8 ± 1.1	3.4 ± 0.2	8.5 ± 0.4	6.3 ± 0.3	71.7 ± 0.6	18[a]	6.0 ± 0.4
4	68.3 ± 0.6	14.9 ± 1.3	3.7 ± 0.3	9.3 ± 0.7	6.7 ± 0.4	67.9 ± 0.7	18.0 ± 1.7	6.0 ± 0.6
5	66.1 ± 0.7	20.6 ± 1.7	2.8 ± 0.2	7.0 ± 0.5	7.3 ± 0.7	67.1 ± 1.5	21.3 ± 3.6	1.8 ± 0.3
6	64.1 ± 0.5	18[a]	4.2 ± 0.2	10.0 ± 0.5	7.2 ± 0.2	60.6 ± 0.4	18[a]	8.9 ± 0.5
	85.1 ± 1.2	18[a]	1.7 ± 0.2	4.2 ± 0.4	7[a]	85.1 ± 3.1	18[a]	1.3 ± 0.3
7	64.3 ± 0.9	18[a]	1.9 ± 0.2	4.8 ± 0.4	7.6 ± 1.7	65.0 ± 3.0	18[a]	1.0 ± 0.4
	92.3 ± 1.7	18[a]	1.0 ± 0.2	2.6 ± 0.4	7[a]	94[a]	18[a]	1.2 ± 0.5
	116.7 ± 1.7	18[a]	1.0 ± 0.2	2.5 ± 0.4	...	...	...	...
8	54.4 ± 1.0	19.1 ± 2.4	2.0 ± 0.2	5.1 ± 0.6	8.7 ± 1.1	53.4 ± 1.4	18.8 ± 3.7	1.6 ± 0.3
	92.9 ± 1.7	18.7 ± 4.0	1.2 ± 0.2	2.9 ± 0.5	7[a]	85[a]	18[a]	0.6 ± 0.2
9	53.8 ± 0.7	18.1 ± 1.6	1.8 ± 0.1	4.4 ± 0.3	10.4 ± 1.4	50.5 ± 1.1	11.0 ± 1.6	0.9 ± 0.2
	89.0 ± 0.8	20.7 ± 2.0	1.8 ± 0.1	4.4 ± 0.4	4.6 ± 2.5	87.1 ± 4.6	18[a]	1.4 ± 1.0
10	51.6 ± 0.9	12.9 ± 2.0	1.5 ± 0.2	3.7 ± 0.5	7[a]	53[a]	15[a]	1.3 ± 0.4
11	15.3 ± 2.1	18[a]	1.6 ± 0.2	2.5 ± 0.4	7.3 ± 1.2	9.3 ± 2.3	18[a]	0.9 ± 0.2
	35.2 ± 1.4	18[a]	1.0 ± 0.2	4.0 ± 0.5	5.8 ± 1.4	36.0 ± 3.0	18[a]	0.9 ± 0.3
12	53.1 ± 1.7	14.4 ± 3.9	1.0 ± 0.2	2.6 ± 0.6	5.7 ± 0.6	57.1 ± 0.9	13.9 ± 2.2	1.5 ± 0.2
13	-0.5 ± 4.0	18[a]	0.4 ± 0.1	1.1 ± 0.4	6.6 ± 1.2	11.6 ± 2.5	18[a]	1.4 ± 0.6
	18.3 ± 2.4	18[a]	1.0 ± 0.1	2.6 ± 0.4	5.1 ± 1.8	27.8 ± 3.4	18[a]	1.2 ± 0.3
	39.1 ± 2.9	18[a]	0.8 ± 0.1	2.0 ± 0.4	5.6 ± 3.6	39[a]	18[a]	1.5 ± 0.6
	57.1 ± 2.5	18[a]	0.7 ± 0.2	1.8 ± 0.4	...	...	...	...

Note. For deriving the column density N_{tot} of $C^{18}O$, the excitation temperature T_{ex} is assumed to be equal to 10 K for all positions and velocity components (see text).
[a] Parameter fixed in the LTE analysis.

Harada et al. (2015) for the H_2 column densities higher than 10^{23} cm^{-2}. The effects of X-rays on the chemistry of the molecular gas are similar to those of cosmic rays (Harada et al. 2015). The cosmic-ray ionization rate ζ is $(4-7) \times 10^{-16}$ s^{-1} in

Sgr B2 (van der Tak et al. 2006; Bonfand et al. 2019), which is 3 orders of magnitude higher than the ζ_X derived for Sgr B2. The very low ζ_X of $\sim 10^{-19}$ s^{-1} shows that the effects of the X-rays on the Sgr B2 molecular gas might be negligible.
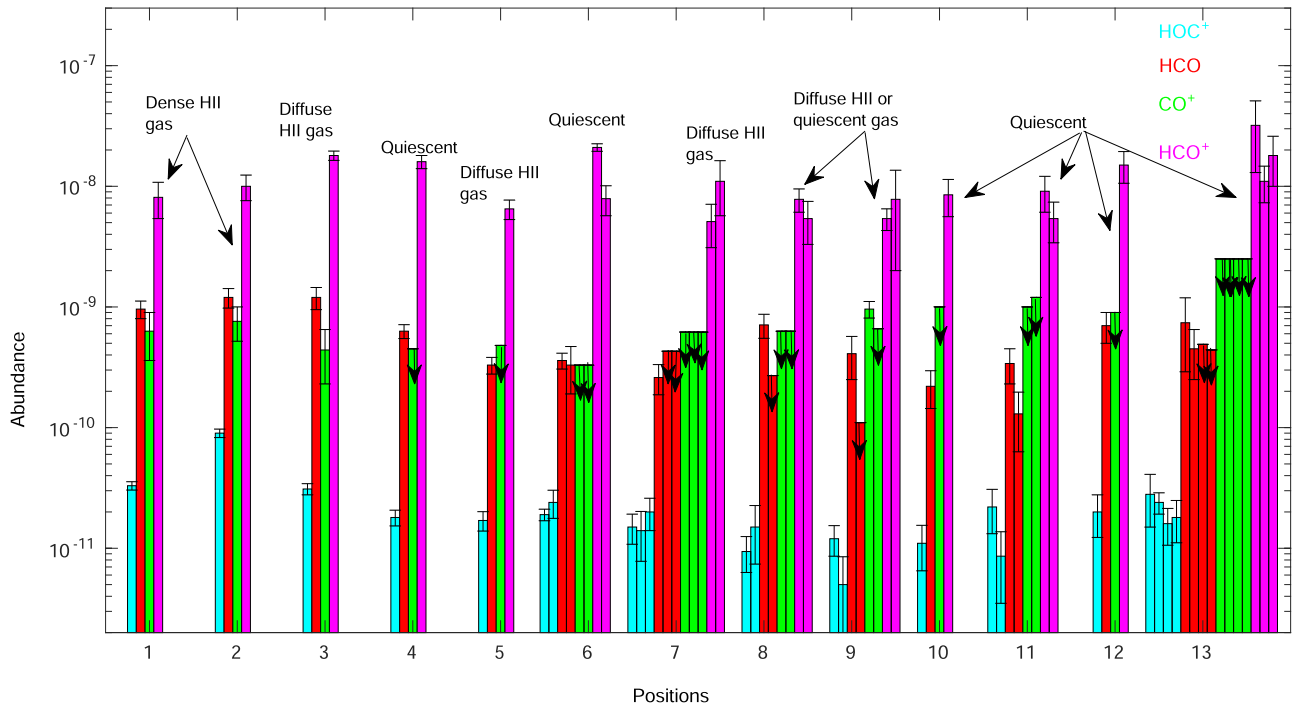
Figure 11. Histogram showing HOC^+ (cyan), HCO (red), CO^+ (green), and HCO^+ (magenta) abundances toward the 13 Sgr B2 positions. More than one bar is used in positions 6–9, 11, and 13, where multiple velocity components of gas are found. In these cases, bars ordered from left to right correspond to gas components ranging from low to high velocities. The gas velocities in these cases can be checked for HOC^+, HCO, and CO^+ in Table 4 and $HC^{18}O^+$ (used to derive the HCO^+ abundances; see Section 4.7) in Table 5. The high-velocity gas of positions 8 and 9 is indeed quiescent gas. Arrows above several bars indicate that these bars represent upper limits on the molecular abundances.
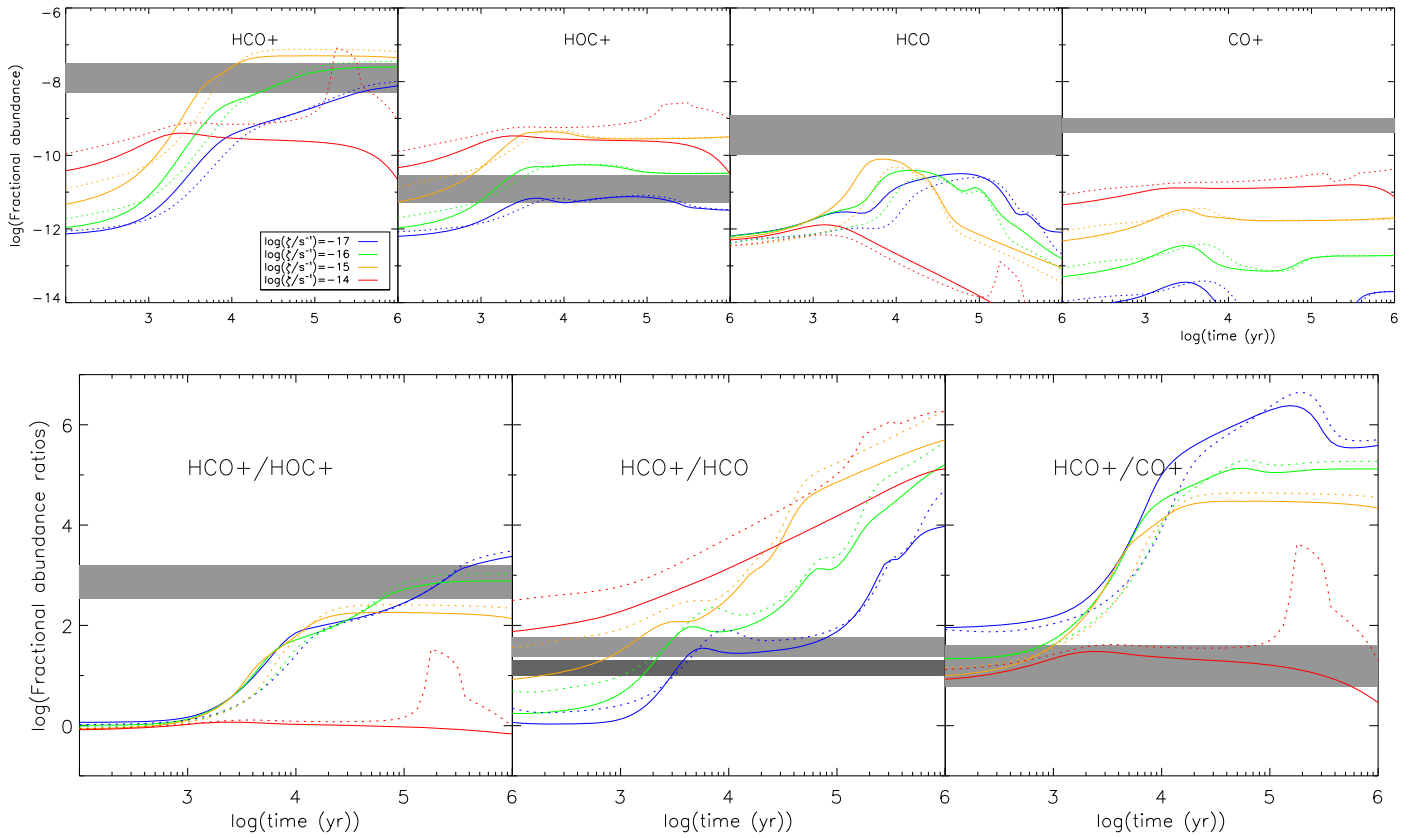
5.2. Molecular Abundances

Figure 11 shows the abundances of HOC^+, HCO, CO^+, and HCO^+ estimated for the 13 positions of Sgr B2. There is more than one bar in positions 6–9, 11, and 13 in this figure because of the multiple velocity components. The gas in positions 1–8 and 10–12 was pervaded by X-rays in 2004, as mentioned in Sections 1 and 3, but from now on, the gas in positions 4 and 10, the high-velocity gas in positions 8 and 9, and the gas in positions 10–12 are considered quiescent, as the effects of the X-rays on the Sgr B2 molecular gas might be negligible, as shown in Section 5.1. The HOC^+ shows the highest abundance of 9×10^{-11} toward position 2 tracing dense H II gas. The low-velocity quiescent gas of position 13 also shows a high abundance of HOC^+, which is a factor of 3.2 lower than that in position 2. This suggests that HOC^+ is formed efficiently in regions affected by UV photons but also through other chemical routes discussed below.

Figure 12 shows fractional abundances of HOC^+, HCO, and CO^+ obtained with the gas-grain time-dependent code Nautilus (Hersant et al. 2009; Semenov et al. 2010). The initial condition for hydrogen is in the molecular form, while for other elements with a higher ionization potential than 13.6 eV, it is in the atomic form, and for all other elements, it is in the ionic form. We ran the model with constant physical conditions. The modeled abundances are obtained for an H_2 density of 10^4 cm^{-3} found toward Sgr B2 (Hüttemeister et al. 1995; Armijos-Abendaño et al. 2015), kinetic temperatures of 50 and 100 K, a visual extinction of 10 mag (implying H_2 column densities of $\sim 10^{22}$ cm^{-2}, values estimated for several Sgr B2 positions as shown in Table 5), and ζ values of 10^{-17}, 10^{-16}, 10^{-15}, and 10^{-14} s^{-1}; ζ values of $(4–7) \times 10^{-16}$ s^{-1} are found toward Sgr B2 (van der Tak et al. 2006; Bonfand et al. 2019). Kinetic temperatures of 50 and 100 K

are included in our chemical modeling because these temperatures are the approximate lower and upper values of the range of kinetic temperatures found for GC molecular clouds, which may be driven by turbulent dissipation and/or cosmic rays (Ao et al. 2013). However, Ginsburg et al. (2016) proposed that turbulent heating is the main heating mechanism of the GC dense gas. Meijerink et al. (2011) predicted gas temperatures of $\sim 100–200$ K for hydrogen column densities $> 10^{22}$ cm^{-2} (as those found for Sgr B2) and ζ values within $5 \times 10^{-17} – 5 \times 10^{-13}$ s^{-1} using PDR models that mimic the effects of cosmic rays and mechanical heating on the gas, but when mechanical heating is not included in the modeling, gas temperatures > 50 K (for hydrogen column densities $> 10^{22}$ cm^{-2}) are only reached for the high ζ values of 5×10^{-14} and 5×10^{-13} s^{-1}, which are at least a factor of 100 higher than that of $\sim 5 \times 10^{-16}$ s^{-1} estimated for Sgr B2 (van der Tak et al. 2006; Bonfand et al. 2019). This contrasts with what was found by Bisbas et al. (2015, 2017), who predicted gas temperatures $\lesssim 50$ K using models with ζ values $\leqslant 10^{-14}$ s^{-1}. Taking into account the ζ value of $\sim 5 \times 10^{-16}$ s^{-1} for Sgr B2, mechanical heating may be the mechanism responsible for increasing the gas temperatures to values > 50 K.

As seen in Figure 12, the HOC^+ abundance increases as the value of ζ increases. Figure 12 shows differences of more than 1 order of magnitude in the HOC^+ abundances predicted by the models with the same ζ value of 10^{-14} s^{-1} but different kinetic temperatures of 50 and 100 K at timescales $> 10^{5.0}$ yr, whereas in the cases with the other ζ values, these differences are of less than a factor of ~ 3 over the timescales of $10^2 – 10^6$ yr. The HOC^+ abundances of $\sim (0.5–2.8) \times 10^{-11}$ are estimated toward the positions of quiescent gas in Sgr B2. Figure 12 shows that the HOC^+ abundances of $\sim (0.5–2.8) \times 10^{-11}$ are reached at timescales lower than $\sim 10^{2.8}$ yr for a ζ value of 10^{-15} s^{-1} or at timescales within $\sim 10^{3.0} – 10^{3.2}$ yr for a ζ value

Figure 12. Fractional abundances (top panels) and ratios (bottom panels) of observed molecules obtained with our chemical modeling for an H_2 density of 10^4 cm^{-3}, kinetic temperatures of 50 (solid lines) and 100 (dotted lines) K, and a visual extinction of 10 mag. The cosmic-ray ionization rate ζ ranges from 1×10^{-17} to 1×10^{-14} s^{-1}. In the top panels, gray bands show the HCO$^+$ abundances of $(0.5–3.2) \times 10^{-8}$ (for the 13 positions), HOC$^+$ abundances of $(0.5–2.8) \times 10^{-11}$ (for quiescent gas), HCO abundances of $(1–12) \times 10^{-10}$ (for diffuse H II and quiescent gas), and CO$^+$ abundances of $(4–10) \times 10^{-10}$ (for dense and diffuse H II gas) estimated in our study (see Section 5.2). In the bottom panels, gray bands show the HCO$^+$/HOC$^+$ ratios of 337–1541 (for quiescent gas); HCO$^+$/HCO ratios of 11–20 and 24–60 for diffuse H II and quiescent gas, respectively; and HCO$^+$/CO$^+$ ratios of 6–41 (for dense and diffuse H II gas) derived in Section 5.3.

of 10^{-16} s^{-1}. Both ζ values are in agreement with those found for Sgr B2 (van der Tak et al. 2006; Bonfand et al. 2019). The highest HOC$^+$ abundance of 2.8×10^{-11} found for the quiescent gas in Sgr B2 is very close to that predicted by models with a ζ value of 10^{-16} s^{-1} and timescales $>10^5$ yr (see Figure 12). Figure 12 also shows HOC$^+$ abundances of $>5 \times 10^{-11}$ for a ζ value of 10^{-14} s^{-1} and different timescales. These HOC$^+$ abundances are at least a factor of $\sim$1.8 higher than the highest HOC$^+$ abundance of 2.8×10^{-11} estimated for the quiescent gas in position 13. Our derived abundances of HOC$^+$ are also consistent with those predicted by models with kinetic temperatures of 50 and 100 K and a ζ value of 10^{-17} s^{-1} at timescales within $\sim$$10^{3.2}$–$10^{5.2}$ yr; however, the ζ value of 10^{-17} s^{-1} is at least a factor of 40 lower than that found in Sgr B2 (van der Tak et al. 2006; Bonfand et al. 2019). This shows that the HOC$^+$ abundances observed in the Sgr B2 quiescent regions are well explained by a high-temperature chemistry and the effects of cosmic rays with ζ values of 10^{-16} and 10^{-15} s^{-1} at different timescales. Both ζ values will be considered in our discussion below.

The HOC$^+$ abundance of 4×10^{-9} is found toward the XDRs in the circumnuclear disk of NGC 1068 (Usero et al. 2004), which is a factor of 143 higher than the highest HOC$^+$ abundance derived for the quiescent regions of Sgr B2, ruling out the effects of X-rays on the molecular gas and consistent with our discussion in Section 5.1.

As seen in Figure 11, the highest HCO abundances of $\sim$$1 \times 10^{-9}$ are found toward position 3, tracing diffuse H II

gas, as well as toward positions 1 and 2, tracing dense H II gas. The HCO also shows high abundances of $\sim$$(3–7) \times 10^{-10}$ for the diffuse H II gas in positions 5, 7, 8, and 9 and $\sim$$(1–7) \times 10^{-10}$ for the quiescent gas in positions 4, 6, and 10–13. This indicates that HCO forms efficiently in gas affected by UV photons but also in quiescent gas. It is believed that photoprocessing of ice mantles and the subsequent photodesorption of HCO or H_2CO (followed by gas phase photodissociation) are responsible for high HCO abundances of $\simeq$$(1–2) \times 10^{-9}$ in PDRs (Gerin et al. 2009), values that are consistent with those of $\sim$$1 \times 10^{-9}$ in positions 1–3.

Chemical modeling of a molecular cloud affected by nondissociative shocks of 10 km s^{-1} shows relative abundances of HCO higher than $\sim$$1 \times 10^{-9}$ starting 10^3 yr after the shock (Mitchell 1984); this is slightly higher than the value of around 7×10^{-10} found for the low-velocity quiescent gas in position 13.

Figure 12 reveals differences of less than a factor of 10 between the HCO abundances predicted by models with the same ζ values of 10^{-16} and 10^{-15} s^{-1} but different kinetic temperatures over timescales of 10^2–10^6 yr. As seen in Figure 12, the highest HCO abundance of $\sim$$8 \times 10^{-11}$ is predicted for a ζ value of 10^{-15} s^{-1}, a kinetic temperature of 50 K, and timescales of $\sim$$10^{3.5}$ yr. This HCO abundance is only a factor of 1.2 lower than that of 1×10^{-10}, but it is a factor of 8.7 lower than the highest abundance of 7×10^{-10} found for the quiescent gas in position 13. This suggests that high-temperature chemistry and cosmic rays are not enough to

Table 6
Ratios of HCO^+ versus HOC^+, HCO, and CO^+

Pos. (Type of Gas) or Source	V_{LSR} (km s^{-1})	HCO^+/HOC^+	HCO^+/HCO	HCO^+/CO^+
1 (dense H II gas)	66	250 ± 82	8 ± 3	13 ± 7
2 (dense H II gas)	65	117 ± 27	9 ± 3	14 ± 5
3 (diffuse H II gas)	72	573 ± 67	14 ± 3	41 ± 20
4 (quiescent gas)	68	887 ± 138	26 ± 4	>36
5 (diffuse H II gas)	67	378 ± 92	20 ± 5	>13
6 (quiescent gas)	61	1117 ± 123	60 ± 9	>66
(quiescent gas)	85	337 ± 123	24 ± 12	>10
7 (diffuse H II gas)	65	353 ± 163	20 ± 9	>8
(diffuse H II gas)	94	791 ± 478	>26	>10
8 (diffuse H II gas)	53	828 ± 304	11 ± 3	>12
(quiescent gas)	85	361 ± 214	>20	>5
9 (diffuse H II gas)	50	465 ± 157	13 ± 6	6 ± 1
(quiescent gas)	87	1541 ± 1563	>72	>12
10 (quiescent gas)	53	791 ± 398	38 ± 17	>8
11 (quiescent gas)	9	405 ± 180	27 ± 10	>8
(quiescent gas)	36	628 ± 432	41 ± 25	>6
12 (quiescent)	57	773 ± 270	22 ± 5	>17
13 (quiescent gas)	12	1143 ± 632	43 ± 30	>13
(quiescent gas)	28	476 ± 157	25 ± 13	>11
(quiescent gas)	39	1169 ± 575	37 ± 21	>14
Prototypical PDRs				
NGC 253	…	80 ± 30[a]	5.2 ± 1.8[a]	38 ± 15[a]
M82	…	60 ± 28[a]	9.6 ± 2.8[a]	32 ± 16[a]
Horsehead	…	75-200[b]	1.1[c]	>1800[b]
Orion bar	…	<166–270[d,e]	2.4[f]	<83–140[d,g]

Notes.
[a] Martín et al. (2009b).
[b] Goicoechea et al. (2009).
[c] Gerin et al. (2009).
[d] Fuente et al. (2003).
[e] Apponi et al. (1999).
[f] Schilke et al. (2001).
[g] Savage & Ziurys (2004).

explain the highest HCO abundances observed in the Sgr B2 quiescent gas and that other mechanisms, such as shocks, are needed to explain those high HCO abundances. It is believed that HCO in hot corinos is formed by the hydrogenation of CO on grains and subsequent thermal desorption in the protostellar phase (Rivilla et al. 2019). This scenario is consistent with what we propose in our paper, with the difference that instead of desorption in the quiescent gas of Sgr B2, the HCO is released to the gas phase through grain sputtering by shocks.

On the other hand, CO^+ line emission is detected only in positions 1–3 and 9 (at gas velocities of ~ 50 km s^{-1}) and without ambiguity only in position 9, as was mentioned before. The CO^+ abundances in these four positions are within $\sim (4$–$10) \times 10^{-10}$. We mentioned in Section 4.2 that the H42α RRL has the highest electron density in position 9 between all the studied positions of diffuse H II gas. This suggests that CO^+ is produced mainly via reactions where UV photons play an important role. This is also supported by the coincidence between the CO^+ relative abundances derived in this paper and those of around 10^{-9} shown by the PDR models of Martín et al. (2009b). Limits lower than $\sim 2 \times 10^{-9}$ are estimated for diffuse H II gas in positions 5, 7, and 8 or quiescent gas in positions 4, 6, and 10–13. The upper limits of these nine positions agree with those lower than $\sim 5 \times 10^{-11}$ obtained for

the four values of ζ shown in Figure 12. This comparison points out that high abundances of CO^+ are expected only in PDRs, as our chemical models including only high-temperature chemistry and cosmic-ray effects show very low CO^+ abundances.

We found differences of less than a factor of 2 in the CO^+ abundances predicted by models with the same ζ values of 10^{-16} and 10^{-15} s^{-1} but different kinetic temperatures of 50 and 100 K over timescales of 10^2–10^6 yr (see Figure 12).

5.3. Column Density Ratios

Column density ratios of HCO^+ versus HOC^+, HCO, and CO^+ for the studied positions of Sgr B2 are given in Table 6. This table lists several velocity components for positions 6–9, 11, and 13 as multiple velocity components of gas are found (see Section 4). The ratios corresponding to NGC 253, M82, Horsehead, and the Orion bar, considered as prototypical PDRs, are included in this table as well (Apponi et al. 1999; Schilke et al. 2001; Fuente et al. 2003; Savage & Ziurys 2004; Goicoechea et al. 2009; Gerin et al. 2009; Martín et al. 2009b). The HCO^+/HOC^+ and HCO^+/HCO ratios as a function of the H_2 column density, the electron density (derived in Section 4.2), and the fluxes of the 6.4 keV Fe line (derived from the 2004 X-ray data in Section 3) for the positions studied
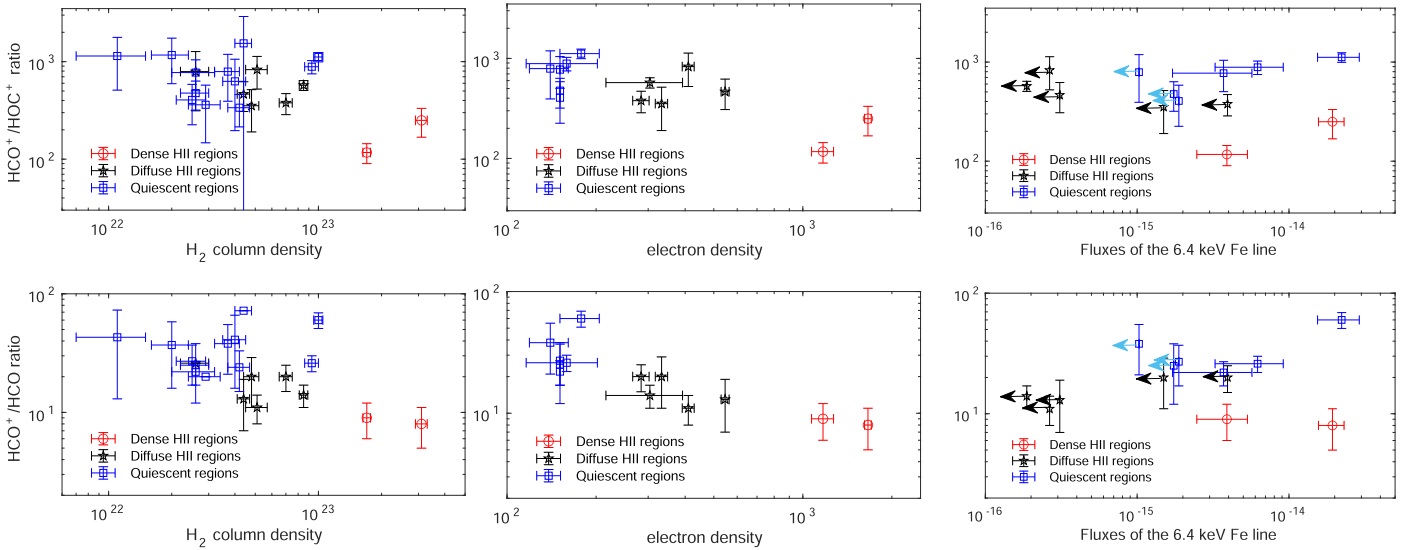
Figure 13. Top panels: HCO^+/HOC^+ ratios for dense and diffuse H II regions, as well as quiescent regions, as a function of the H_2 column density (left panel), electron density (middle panel), and fluxes of the 6.4 keV $K\alpha$ line (right panel). Bottom panels: same as the top panels but for the HCO^+/HCO ratio. Arrows in several panels show lower or upper limits. The middle and right panels show fewer values than the left panel, as the ionized gas does not have a molecular counterpart in all velocity components (see Section 4.2) and the fluxes of the 6.4 keV Fe line are represented only for the lowest-velocity components in positions where multiple velocity components of gas are found.

in our paper are displayed in Figure 13. The lowest HCO^+/HOC^+ ratios of 117–250 are found in positions 1 and 2, while the other positions tracing diffuse H II regions or quiescent gas show HCO^+/HOC^+ ratios higher than 337. The bottom panels of Figure 13 show that there is a good correlation between the HCO^+/HCO ratio and both the H_2 column density and the electron density. Figure 13 also shows that there is no correlation between the 6.4 keV Fe $K\alpha$ line flux and both the HCO^+/HOC^+ and HCO^+/HCO ratios.

Figure 13 shows similar values of the HCO^+/HOC^+ ratios in both diffuse H II and quiescent regions. The HCO^+/HOC^+ ratios of 117–250 agree with those of <270 of prototypical PDRs (see Table 6). Based on this, the HCO^+/HOC^+ ratio seems to be a good tracer of dense H II regions where UV photons dominate the heating and chemistry of the molecular gas, but it does not allow one to distinguish between quiescent gas and diffuse ionized gas.

The bottom panels of Figure 12 show the HCO^+/HOC^+, HCO^+/HCO, and HCO^+/CO^+ ratios obtained with our chemical modeling. We believe that the agreement of the HCO^+/HOC^+ ratios of 337–1541 estimated for the Sgr B2 quiescent regions is better for $\zeta = 10^{-16}\,\mathrm{s}^{-1}$, as this ζ value agrees better with that of $4 \times 10^{-16}\,\mathrm{s}^{-1}$ found for the Sgr B2 envelope and timescales $>10^{4.5}$ yr. This is consistent with what was discussed in Section 5.2 and implying that the values of $\zeta = 10^{-16}\,\mathrm{s}^{-1}$ and timescales $>10^{5.0}$ yr give a better agreement with the observations. For these values, our model reveals HCO^+ abundances of $\sim 1 \times 10^{-8}$ that agree with those of $(0.5$–$3.2) \times 10^{-8}$ estimated for Sgr B2 (see Figure 12).

As seen in Figure 13, the HCO^+/HCO ratio also shows the lowest values within 8–9 in positions 1 and 2 tracing dense H II gas. On the other hand, the HCO^+/HCO ratios within 11–20 and 24–60 are found in diffuse H II gas and quiescent gas, respectively. It is clear in Figure 13 that this ratio shows a range of higher values in quiescent regions than in regions of diffuse H II gas, implying that the HCO^+/HCO ratio is a good tracer of regions affected by UV photons, as well as the HCO^+/HOC^+

ratio, but that this ratio is also sensitive to the electron density of the ionized gas. The HCO^+/HCO ratios of 24–60 found for quiescent gas agree with those estimated for a ζ value of $10^{-15}\,\mathrm{s}^{-1}$, kinetic temperatures of 50 and 100 K, and timescales $<10^{3.1}$ yr or a ζ value of $10^{-16}\,\mathrm{s}^{-1}$, kinetic temperatures of 50 and 100 K, and timescales within $10^{3.1}$–$10^{3.2}$ yr. It is important to stress that the agreement of the modeled ratios for the above ζ and timescales with those derived is due to both the modeled HCO^+ and HCO abundances being the same orders of magnitude lower than those found for the quiescent gas (see Figure 12).

The HCO^+/HCO ratios within 8–9 derived for positions 1 and 2 are in agreement with those of the starburst galaxies NGC 253 and M82 (Martín et al. 2009b).

On the other hand, we were able to derive HCO^+/CO^+ ratios only for positions 1–3 and 9, where CO^+ emission was detected. We estimated lower limits on the HCO^+/CO^+ ratio for the other positions. As we can see in Table 6, the HCO^+/CO^+ ratio is also a good tracer of regions affected by UV photons, as this ratio is within 6–14 in positions 1, 2, and 9, where we found the highest electron densities among all of the studied regions (see Section 4.2), while the HCO^+/CO^+ ratio of 41 is derived for the diffuse ionized gas in position 3. The HCO^+/CO^+ ratio of 41 found for position 3 is reached at timescales lower than $\sim 10^{3.0}$ yr for ζ values of 10^{-16} and $10^{-15}\,\mathrm{s}^{-1}$ (see Figure 12). However, this agreement is due to both the modeled HCO^+ and CO^+ abundances being the same orders of magnitude lower than the derived values, as in the case of the HCO^+/HCO ratio.

Martín et al. (2009b) found HCO^+/CO^+ ratios of 32 ± 16 and 38 ± 15 for M82 and NGC 253, respectively, which are between the values found for the dense and diffuse H II regions. The upper limit of <83–140 on the HCO^+/CO^+ ratio found for the Orion bar (Savage & Ziurys 2004; Fuente et al. 2006) is also consistent with those within 6–41 estimated toward positions 1–3 and 9.

6. Conclusions

In this paper, we compared SiO $J = 2-1$ emission maps with X-ray maps observed in 2004 and 2012 toward Sgr B2. Integrated intensity maps of HCO $1_{0,1}-0_{0,0}$ ($J = 3/2-1/2$, $F = 2-1$) and H^{13}CO$^+$ $J = 1-0$ toward Sgr B2 are also presented. Three large X-ray spots are observed in the X-ray map of 2004; two of them were identified and studied by Terrier et al. (2018), while the other is identified in this paper and called G0.69–0.11. We also found that the known spot G0.66–0.13 observed in the 2012 X-ray map is apparently associated with a southeast region being part of a shell shown by the SiO $J = 2-1$ emission at velocities of 15–25 km s^{-1}. In addition, we derived Fe Kα line fluxes or limits on the fluxes toward 13 positions of Sgr B2. Twelve of these sources are affected by UV photons and/or X-rays, whereas the other remaining source is quiescent. The molecular gas in these Sgr B2 positions was irradiated by a field of X-rays lower than $10^{37.09}$ erg s^{-1} until 2012. We derived an X-ray ionization rate of $\sim 10^{-19}$ s^{-1} for Sgr B2, a very low value to affect the chemistry of the molecular gas.

Our study of the H42α RRLs and the derived electron density allowed us to classify the sources associated with H II regions into regions of diffuse and dense hydrogen ionized gas. We found abundances of HOC$^+$, HCO, and CO$^+$, as well as the HCO$^+$/HOC$^+$, HCO$^+$/HCO, and HCO$^+$/CO$^+$ ratios for the 13 positions, which were compared with those obtained with chemical modeling. We found that a model including high-temperature chemistry, cosmic rays with an ionization rate of 10^{-16} s^{-1}, and timescales $>10^{5.0}$ yr gives a better agreement with the HOC$^+$ abundances derived for the quiescent gas of Sgr B2. Apart from high-temperature chemistry and cosmic rays, shocks have to be invoked to explain the highest HCO abundances observed in the Sgr B2 quiescent gas. On the other hand, CO$^+$ emission is not detected toward quiescent regions, indicating that high abundances of CO$^+$ are expected only in PDRs.

We found differences of less than a factor of 3, 10, and 2 between the abundances of HOC$^+$, HCO, and CO$^+$, respectively, predicted by models with the same cosmic-ray ionization rates of 10^{-16} and 10^{-15} s^{-1} but different kinetic temperatures of 50 and 100 K over timescales of 10^2–10^6 yr.

The lowest values of the HCO$^+$/HOC$^+$, HCO$^+$/HCO, and HCO$^+$/CO$^+$ ratios are found in positions of Sgr B2 tracing dense H II gas, which shows that these ratios are good tracers of regions where UV photons dominate the heating and chemistry of the molecular gas. The HCO$^+$/HCO ratio is sensitive to the electron density of ionized regions, as it shows values within 12–18 and 7–9 for diffuse and dense H II regions, respectively, whereas HCO$^+$/HCO ratios within 27–60 are estimated for the quiescent gas of Sgr B2. We found a good correlation between the HCO$^+$/HCO ratio and both the H$_2$ column density and the electron density.

ORCID iDs

J. Armijos-Abendaño ● https://orcid.org/0000-0003-3341-6144
M. Llerena ● https://orcid.org/0000-0003-1354-4296
S. Martín ● https://orcid.org/0000-0001-9281-2919

References

Aladro, R., König, S., Aalto, S., et al. 2018, A&A, 617, A20
Aladro, R., Martín, S., Riquelme, D., et al. 2015, A&A, 579, A101
Aladro, R., Martín-Pintado, J., Martín, S., et al. 2011, A&A, 525, A89
Amo-Baladrón, M. A., Martín-Pintado, J., & Morris, M. R. 2009, ApJ, 694, 943
Ao, Y., Henkel, C., Menten, K. M., et al. 2013, A&A, 550, A135
Apponi, A. J., Pesch, T. C., & Ziurys, L. M. 1999, ApJL, 519, L89
Armijos-Abendaño, J., López, E., Martín-Pintado, J., et al. 2018, MNRAS, 476, 2446
Armijos-Abendaño, J., Martín-Pintado, J., Requena-Torres, M. A., et al. 2015, MNRAS, 446, 3842
Bally, J., Stark, A. A., Wilson, R. W., & Henkel, C. 1987, ApJ, 65, 13
Belloche, A., Müller, H. S. P., Menten, K. M., et al. 2013, A&A, 559, A47
Bisbas, T. G., Papadopoulos, P. P., & Viti, S. 2015, ApJ, 803, 37
Bisbas, T. G., van Dishoeck, E. F., Papadopoulos, P. P., et al. 2017, ApJ, 839, 90
Boehle, A., Ghez, A. M., Schödel, R., et al. 2016, ApJ, 830, 17
Bonfand, M., Belloche, A., Garrod, R. T., et al. 2019, A&A, 628, A27
Frerking, M. A., Langer, W. D., & Wilson, R. W. 1982, ApJ, 262, 590
Fuente, A., García-Burillo, S., Gerin, M., et al. 2006, ApJL, 641, L105
Fuente, A., Rodríguez-Franco, A., García-Burillo, S., Martín-Pintado, J., & Black, J. H. 2003, A&A, 406, 899
Gerin, M., Goicoechea, J. R., Pety, J., et al. 2009, A&A, 494, 977
Ginsburg, A., Henkel, C., Ao, Y., et al. 2016, A&A, 586, A50
Goicoechea, J. R., Cuadrado, S., Pety, J., et al. 2017, A&A, 601, L9
Goicoechea, J. R., Pety, J., Gerin, M., et al. 2009, A&A, 498, 771
Harada, N., Riquelme, D., Viti, S., et al. 2015, A&A, 584, A102
Hersant, F., Wakelam, V., Dutrey, A., et al. 2009, A&A, 493, L49
Hüttemeister, S., Wilson, T. L., Mauersberger, R., et al. 1995, A&A, 294, 667
Jiménez-Serra, I., Martín-Pintado, J., Rodríguez-Franco, A., et al. 2007, ApJL, 661, L187
Kawamuro, T., Izumi, T., & Imanishi, M. 2019, PASJ, 71, 68
Maloney, P. R., Hollenbach, D. J., & Tielens, A. G. G. M. 1996, ApJ, 466, 561
Martín, S., Kohno, K., Izumi, T., et al. 2015, A&A, 573, A116
Martín, S., Martín-Pintado, J., Blanco-Sánchez, C., et al. 2019, A&A, 631, A159
Martín, S., Martín-Pintado, J., & Mauersberger, R. 2009a, ApJ, 694, 610
Martín, S., Martín-Pintado, J., & Viti, S. 2009b, ApJ, 706, 1323
Martín, S., Requena-Torres, M. A., Martín-Pintado, J., et al. 2008, ApJ, 678, 245
Meijerink, R., Spaans, M., Loenen, A. F., & van der Werf, P. P. 2011, A&A, 525, A119
Mitchell, G. F. 1984, ApJS, 54, 81
Rivilla, V. M., Beltrán, M. T., Vasyunin, A., et al. 2019, MNRAS, 483, 806
Rivilla, V. M., Jiménez-Serra, I., Zeng, S., et al. 2018, MNRAS, 475, L30
Salak, D., Tomiyasu, Y., Nakai, N., et al. 2018, ApJ, 856, 97
Savage, C., & Ziurys, L. M. 2004, ApJ, 616, 966
Schilke, P., Pineau des Forêts, G., Walmsley, C. M., & Martín-Pintado, J. 2001, A&A, 372, 291
Semenov, D., Hersant, F., & Wakelam, V. 2010, A&A, 522, A42
Spaans, M., & Meijerink, R. 2007, ApJL, 664, L23
Terrier, R., Clavel, M., Soldi, S., et al. 2018, A&A, 612, A102
Terrier, R., Ponti, G., Bélanger, G., et al. 2010, ApJ, 719, 143
Treviño-Morales, S. P., Fuente, A., Sánchez-Monge, Á., et al. 2016, ApJL, 593, L12
Usero, A., García-Burillo, S., Fuente, A., et al. 2004, A&A, 419, 897
van der Tak, F. F. S., Belloche, A., Schilke, P., et al. 2006, A&A, 454, L99
Wilson, T. L., & Rood, R. T. 1994, ARA&A, 32, 191
Yusef-Zadeh, F., Hewitt, J. W., & Cotton, W. 2004, ApJS, 155, 421
Ziurys, L. M., & Apponi, A. J. 1995, ApJL, 455, L73